Thesis for the degree
Master of Science

Submitted to the Scientific Council of the
Weizmann Institute of Science
Rehovot, Israel

עבודת גמר (תזה) לתואר
מוסמך למדעים

מוגשת למועצה המדעית של
מכון ויצמן למדע
רחובות, ישראל

By

Ariel Smooha

מאת

אריאל שמוחה

השפעת ההקרנה בלייזר על מתייגי ספין במגנטומטר מבוסס-יהלום

The influence of laser irradiation on spin labels in diamond magnetometry

Advisor:

Dr. Amit Finkler

מנחה:

ד"ר עמית פינקלר

September 2021

תשרי ה'תשפ"ב

Abstract

In order to understand the functionality of bio-molecules, it is crucial to use structural analysis with conventional techniques such as X-ray crystallography, cryo-electron microscopy, and NMR spectroscopy. However, with these techniques, sample preparation and data analysis of some bio-molecules might be complicated and even impossible in some cases. A solution, in this case, can be the electron paramagnetic resonance (EPR) spectroscopy technique. In this way, by appending a spin-label (a spin system that includes an unpaired valence electron) to a molecule of biological importance, we can gain information on the labeled target molecule structure and can also get information regarding the local environment from the spectra. However, conventional EPR measurements require averaging over a large number of spins and are limited to a macroscopic sample volume. Thus, it is not trivial to obtain information regarding different structural configurations in inhomogeneous samples, where a nanometer resolution is required. Here, the nitrogen-vacancy (NV) center, which is a fluorescent crystal defect in diamond, comes into play and can be utilized to solve this issue as it can function as a nano-scale EPR sensor. However, the NV readout scheme is based on confocal microscopy, which entails the use of a highly focused laser beam. Because the laser's beam is focused to a spatial resolution of microns, the material is exposed to a relatively high laser power density which might be harmful to it.

In this thesis, I investigated the influence of laser irradiation on spin-labeled molecules in diamond magnetometry by detecting their behavior using designated pulse sequences that enable it. We successfully synthesized spin-labeled poly-L-lysine molecules, using OXYL-1-NHS as a spin label, and used the drop-casting method to apply the material in a relatively high spatial resolution in order to investigate the spin labels via NV-based EPR spectroscopy. We utilized confocal imaging and double electron-electron resonance (DEER) pulse sequences in a homemade setup in order to examine and understand the influence of laser irradiation on the spin labels.

List of Abbreviations

AC	alternating current
APD	avalanche photodiode
CVD	chemical vapor deposition
CW	continuous wave
DC	direct current
DEER	double electron-electron resonance
EPR	electron paramagnetic resonance
ESR	electron spin resonance
FFT	fast Fourier transformation
FID	free induction decay
HPHT	high pressure high temperature
ISC	inter system crossing
MW	microwave
NMR	nuclear magnetic resonance
NV center	nitrogen vacancy center in diamond
ODMR	optically detected magnetic resonance
PLL	poly-L-lysine
PL	photoluminescence
RT	room temperature
SL	spin label
ZFS	zero field splitting

Contents

Abstract i

List of Abbreviations ii

Table of Contents iii

Introduction iv

1 The Nitrogen-Vacancy Center In Diamond 1
- 1.1 Diamond . . . 1
- 1.2 The NV Center . . . 1
- 1.3 Spin Hamiltonian . . . 5
- 1.4 Pulse sequences . . . 6
  - 1.4.1 Optically Detected Magnetic Resonance (ODMR) . . . 8
  - 1.4.2 Pulsed ODMR . . . 9
  - 1.4.3 Rabi Oscillations . . . 12
  - 1.4.4 Ramsey Interferometry . . . 12
  - 1.4.5 Spin Echo (Hahn Echo) . . . 14
  - 1.4.6 Double Electron-Electron Resonance (DEER) . . . 16

2 Experimental Setup 18
- 2.1 Room temperature magnetometer setup . . . 18
- 2.2 Confocal microscopy with nitrogen-vacancy centers . . . 18
- 2.3 Microwave radiation . . . 18

3 EPR Spectroscopy of the Spin Labels 20
- 3.1 Sample preparation . . . 20
  - 3.1.1 Spin labeling of poly-L-lysine . . . 20
  - 3.1.2 Diamond sample preparation . . . 21
- 3.2 Nanoscale EPR experiments . . . 22
  - 3.2.1 Applying the DEER sequence . . . 22
  - 3.2.2 ESR for nitroxide spin labels via NV centers . . . 24
  - 3.2.3 Effect of laser irradiation . . . 27

4 Summary and Discussion 29

5 Appendix 30
- 5.1 Raman spectroscopy measurements . . . 30
- 5.2 X-ray photoelectron spectroscopy (XPS) measurements . . . 32

References 42

Acknowledgements 43

Introduction

To understand the functionality of bio-molecules, it is crucial to use structural analysis, since spatial conformation determines the functionality of proteins within biological systems. There are four levels of protein structures: Primary, Secondary, Tertiary, and Quaternary. The primary structure is determined by the sequence of amino acids constructing the molecule. The secondary structure is determined by the dihedral angles of the peptide bonds. The tertiary structure is determined by the folding of the protein in space, and the quaternary structure is determined by the association of folded molecules to complex functional proteins. Due to this complexity, it is difficult to infer the folded shape of the proteins based on the chemical formula. Therefore, there is a great interest in methods that enable to infer the structure of these molecules. Techniques that are commonly used for this purpose are X-ray crystallography [1, 2], cryo-electron microscopy, and NMR spectroscopy [3]. By using these methods, one can obtain the complete three-dimensional structure of a studied bio-molecule. However, these methods have high requirements in sample preparation and data analysis, where the analysis of some bio-molecules is impossible.

A solution, in this case, can be the electron paramagnetic resonance (EPR) spectroscopy technique. In this case, spin labels, each has an unpaired valence electron, are attached to specific sites in the target molecule. This process is called site-directed spin labeling (SDSL). By investigating the spin coupling between nearby spin labels, one can infer the distance between them with a small-scale prediction of nanometers [4]. In this way, by appending a paramagnetic fragment (a 'spin label') to a molecule of biological importance, we can gain information on the labeled target molecule structure. Moreover, from the spectra, one can also get information about the local environment. Conventional EPR measurements, which were also performed in this thesis, require averaging over a relatively large number of spins and are limited to a macroscopic sample volume ($\sim$ µm^3). Thus, it is not easy to gain information regarding different structural configurations in inhomogeneous samples. These issues can be solved by utilizing the NV center, which can function as a nanoscale EPR sensor.

EPR spectroscopy via NV centers was already performed for the detection of several electronic species such as nitrogen defects [5, 6], radicals [7, 8], NV centers [8], and spin labeled proteins [9, 10]. A main target which is still an elusive goal is measuring the magnetic resonance spectrum of single bio-molecules. Obtaining a signal from a single bio-molecule is essential for revealing their structure and dynamics.

For performing sensing measurements with NVs, a green excitation laser is focused on the sample (containing the NV center and the spin-labeled molecule) using a confocal microscopy setup. Consequently, the spin-labeled molecule is exposed to a relatively high laser power density of $\sim 1 \times 10^9$ W/m^2 (For comparison, the power density from the sun's radiation

is $\sim 1.4 \times 10^3$ W/m^2) which might harm it and bring about its decomposition during the measurement. Therefore, in this thesis, I investigated the influence of laser irradiation on spin-labeled molecules for enabling optimal measurement conditions. To investigate the effect of laser irradiation on the spin labels, it is crucial to detect them by NV-based EPR spectroscopy, which was performed in this work. The thesis is organized as follows. In Sec. 1, I will discuss the properties of the NV center, the system Hamiltonian, and the relevant pulse sequences performed in this thesis utilizing NV centers. In Sec. 2, I will present and explain the experimental setup with NV centers. In Sec. 3, I will discuss the obtained general results and the specific results from NV-based EPR spectroscopy, and in Sec. 4, I will summarize and discuss the results.

1 The Nitrogen-Vacancy Center In Diamond

1.1 Diamond

Diamond is one of the allotropes of pure carbon. It has extraordinary properties, such as being the hardest natural material and having the highest thermal conductivity of any natural material. Moreover, it has a relatively high refractive index. Diamond is a single crystal in which the carbon atoms are covalently bonded, creating a tetrahedral lattice structure with an sp^3 orbital hybridization of the carbons. The diamond cubic unit cell is based on the face-centered cubic (FCC) Bravais lattice. It has a basis of two carbon atoms at $(0, 0, 0)$ and $(a/4, a/4, a/4)$ where a, the edge length, equals 3.57 Å. Diamond is a semiconductor with a bandgap of 5.47 eV [11], and optical properties of transmission across the ultraviolet (UV) to Infrared (IR) range, which makes it also useful for optical applications in addition to its mechanical ones, thus, allowing the observation of single color centers such as the NV center, which is embedded in the diamond lattice structure. This specific crystal defect makes the diamond a fascinating platform for quantum devices utilization.

Because of the spectacular characteristics of the diamond, it is widely used in industry and science facilities. Specifically, in this work, synthesized diamonds were used. Such a single crystal diamond can be synthesized in two methods: the High-Pressure High-Temperature (HPHT) method and the Chemical Vapor Deposition (CVD) method. In the first method, machines compress graphite at high temperatures to transform into diamond [12], and in the second method, methane plasma is utilized to grow new diamond layers upon an existing diamond seed [13].

1.2 The NV Center

The nitrogen-vacancy (NV^-) center is an optically active defect in diamond. The NV^- center is being widely studied due to its possible application in quantum information processing (QIP) and magnetometry, where we can reach room temperature (RT) DC and AC magnetic field sensitivities of $\sim 1\ \mu T/\sqrt{Hz}$ and $\sim 1\ nT/\sqrt{Hz}$, respectively [14, 15]. The defect consists of a substitutional nitrogen atom in the crystal with a vacancy at the adjacent lattice site, as shown in Fig. 1a. Each NV^- center's symmetry axis is constrained to lie along with one of the four [111] crystallographic directions. The NVs can be observed to exist in three charge states: NV^-, NV^0, and NV^+. However, only the negatively charged NV^- center is favored for applications in quantum information and quantum sensing [16]. The NV^- center has a C_{3v} symmetry and is comprised of a six-electron system (NV^- will be denoted as NV in the following, for convenience and clarity). NV centers are very appealing due to a number of reasons [17]. First, it is because of the possibility to control the defect density to a level where only one is present within a laser spot, making it possible to study the properties of a single

NV center. And secondly, the fact that the NV center forms a two-level manifold quantum system (see Sec. 1.3) that can serve as a quantum bit ('qubit'). The NV defect exhibits a spin = 1 triplet electronic ground state with relatively long spin lifetimes at RT [15, 18, 19]. Its spin energy levels are sensitive to magnetic fields, electric fields, strain, and temperature variations [16], making the NV a multimodal sensor.

The NV's electronic structure has been being studied extensively, both experimentally and theoretically, and there are several reports dealing with and explaining its fascinating properties [20–24]. The basic photophysics of the NV center, underlying its properties, can be explained by four electronic levels: the ground state of symmetry $^3A_2$, the excited state of symmetry ^3E, and the metastable singlet state that involves two levels with symmetries $^1A_1$ and ^1E as depicted in Fig. 1b. The first two states are spin triplets and further split into three spin sub-levels with $m_s = 0$, $m_s = +1$, and $m_s = -1$. Here, the m_s denotes the spin projection along the quantization axis of the NV defect, which joins the nitrogen and the vacancy ([111] axis). The sublevels of the $^3A_2$ state are split in energy by spin-spin interaction into the $m_s = 0$ and the degenerate $m_s = \pm 1$ states. In the absence of a magnetic field, these levels are separated by $D = 2.87$ GHz, known as the zero-field splitting (ZFS) term. The defect can be optically excited to the triplet ^3E level through a spin conserving transition. This level has similar properties as the triplet ground state except for the ZFS, which is $D_{es} = 1.42$ GHz in this case. The transition from the excited state to the ground state exhibits a broadband PL emission (wavelengths of 650 - 800 nm, corresponding to 1.549 eV - 1.907 eV) with a zero-phonon line (ZPL) at 637 nm (1.945 eV) [25]. Interestingly, it can be excited through a non-resonant illumination at wavelengths below it (520 nm, for instance, due to phonon-coupling processes) [22]. Once excited to the ^3E level, the NV center can relax through a radiative transition which produces a broadband red PL or through a secondary path involving non-radiative intersystem crossing (ISC) to the $^1A_1$ and the ^1E singlet states [26, 27]. The characteristics (relative energies and number of states) of these singlet states are still under debate and matter of investigation [28]. These levels play a crucial role in the NV's spin dynamics. The optical transitions are mainly spin conserving, i.e., $\Delta m_s = 0$. On the other hand, ISCs to the ^1E singlet state are more probable from the $m_s = \pm 1$ sublevel and much less probable from the $m_s = 0$ sublevel. Conversely, the decay from the lowest $^1A_1$ singlet level is preferable to the $m_s = 0$ sublevel. These spin selective processes enable the polarization of the NV into the $m_s = 0$ sub-level by optical pumping. Since the ISCs are non-radiative, the PL intensity is higher when this state is populated. This produces both spin state-dependent fluorescence contrast and optical spin initialization into the NV's $m_s = 0$ ground state. Effective optical initialization and readout of NVs do not require the use of narrow-linewidth lasers, and a single 520 nm solid-state laser is sufficient, as discussed.

NVs can operate at ambient temperatures, pressures, and magnetic fields and thus require

no cryogenics, vacuum system, or high magnetic bias field in the tesla range. Moreover,

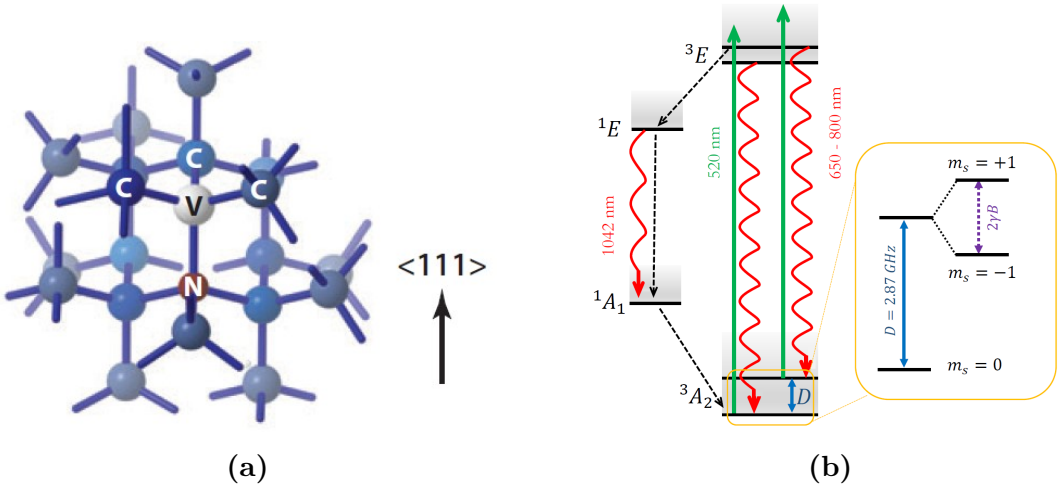

(a) **(b)**

Figure 1: The NV center. **(a)** The lattice structure of the NV center [29]. **(b)** Energy level scheme of NV^-. Wiggly and straight arrows indicate the radiative transitions, and the dashed arrows indicate nonradiative decay via the singlet state. One can observe the three spin sublevels with $m_s = 0$ and $m_s = \pm 1$. D is the zero-field splitting (ZFS), and $2\gamma B$ is the *Zeeman* splitting ($\gamma = g\mu_B$, the electron gyromagnetic ratio).

they also do not suffer from photobleaching or blinking as often observed for solid-state emitters like dye molecules [30] or quantum dots [31] under ambient conditions. Because of the properties of diamonds described in the previous section (Sec. 1.1) and the fact that it is chemically inert, it is very stable. Thus, the combination of these properties makes the NV an attractive candidate in biological systems [29, 32–37]. Furthermore, the presented properties of the NV and its angstrom scale size enable nanometer-scale spatial resolution [38, 39].

The diamond used in this work contains on average NVs with a concentration of 1 NV per μm^2. These NV centers are oriented at all four crystallographic orientations. Every orientation is sensitive to a magnetic field projection along its axis ($B_\parallel$) and perpendicular to it ($B_\perp$). This is depicted in Fig. 1.2, where one can observe the four different possible orientations of the NV axis. The bright spot (high PL contrast, in yellow) in each sub-figure indicates the XY coordinates of the static magnet where its induced magnetic field is aligned with the NV axis. At the spots where it is not aligned, we have perpendicular components of the magnetic field ($B_\perp$) such that the PL is weakened (low PL contrast, in blue) due to field-induced spin level mixing that increases the probability for non-radiative ISC transitions [40].

NVs can be used as ensembles or as single defect magnetometers. In this thesis, as will be shown, signals were obtained from single emitters.

Due to the fact that the defect's luminescence is spin-dependent, it can be used for magnetic field sensing and the detection of nearby paramagnetic species [41]. Because of the high sensitivity of the NV center to external magnetic fields, measurements can also be performed

on single spins, such as spin labels (SL), that are localized within a few nanometers [7–9, 42, 43].

This exciting aspect of the NV center is of our interest, and for such measurements, a green excitation laser is focused on a sample containing a single NV center and a spin-labeled molecule using a confocal microscope setup, as will be described in the following sections.

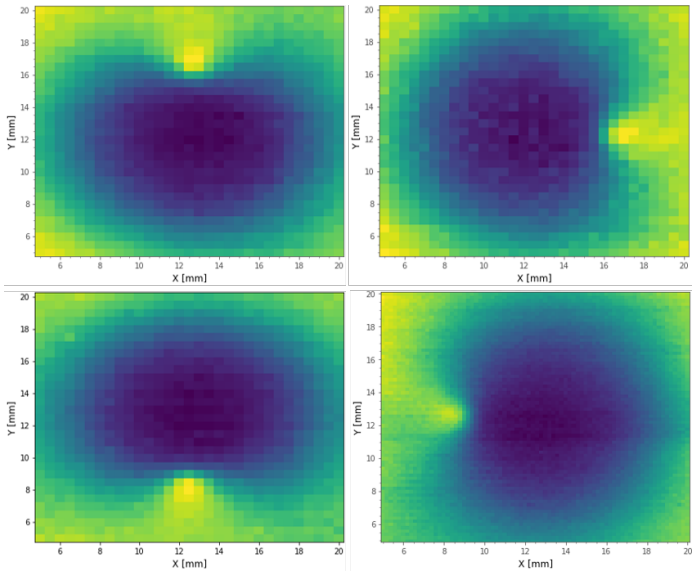

Figure 1.2: Magnet scan. Contrast image of the PL as a function of the static magnet coordinates. The four possible orientations of the NV center can be observed very clearly. One can observe that when the magnet is not aligned with the NV axis, the PL decreases due to perpendicular ($B_\perp$) magnetic field components, which bring to field-induced spin level mixing that increases the probability for non-radiative ISC transitions [40]. The magnet is located at the height of 4 mm from the diamond surface. The magnetic field in the case that the magnet is aligned is approximately 220 Gauss.
The script for the magnet scan was written by *Dan Yudilevich* from our group.

1.3 Spin Hamiltonian

The following equation gives the simplified Hamiltonian of the ground state of the NV spin system

$$\hat{\mathcal{H}} = D\hat{S}_z^2 + \gamma_e B \cdot \hat{S} + \hat{S} \cdot A \cdot \hat{I} \tag{1.1}$$

$D = 2.87$ GHz is the zero-field splitting (ZFS), $\gamma_e = 28$ GHz T^{-1} is the gyromagnetic ratio of the NV electron spin, $\hat{S}$ is the spin operator of the electron spin, $\hat{I}$ is the spin operator of the nitrogen nuclear spin, and A is the hyperfine tensor defining the interaction between the NV electron spin and the nitrogen nuclear spin. The first term of this equation is derived, as explained, from the ZFS, which is a consequence of internal interactions in the diamond lattice to which the NV is exposed. The second component describes the interaction between an external magnetic field and the NV electron spin and is known as Zeeman splitting. In this work, the DC magnetic field is aligned with the NV axis, denoted as the z-axis. Thus, the Zeeman splitting term, in this case, is simplified to the form: $\hat{\mathcal{H}}_{Zeeman} = \gamma_e B_z \cdot \hat{S}_z$. The eigenstates of the Hamiltonian (without the hyperfine term) are $|m_s = 0\rangle$, $|m_s = +1\rangle$ and $|m_s = -1\rangle$, with eigenvalues 0, $+\gamma_e B_z$, and $-\gamma_e B_z$ respectively. In effect, the magnetic field induces the separation between the $|m_s = +1\rangle$ and $|m_s = -1\rangle$ levels by $2\gamma_e B_z$ (as can be seen in Figure 1.4c). The last component of the Hamiltonian is the hyperfine interaction term which describes the interaction between the NV electron spin and the nitrogen nuclear spin. Since A, the hyperfine tensor, is diagonal and the non-axial magnetic hyperfine parameters are equal, the hyperfine Hamiltonian is given by [16]

$$\hat{\mathcal{H}}_{Hyperfine} = A^{||}\hat{S}_z + A_{\perp}\left[\hat{S}_x\hat{I}_x + \hat{S}_y\hat{I}_y\right] \tag{1.2}$$

The first term leads to the hyperfine coupling of the $|m_s = \pm 1\rangle$ spin states while the other term induces flip-flop events of the electron and nuclear spins as can be inferred from the equivalent hyperfine Hamiltonian expressed with the spin ladder operators

$$\hat{\mathcal{H}}_{Hyperfine} = A^{||}\hat{S}_z + \frac{A_{\perp}}{2}\left[\hat{S_+}\hat{I_-} + \hat{S_-}\hat{I_+}\right] \tag{1.3}$$

The value of the tensor elements is dependent on the nitrogen isotope type. In the case that we have an ^{15}N atom which has a nuclear spin of $I = \frac{1}{2}$, we will get a separation of the spin state into two sub-levels following the simple formula $2I + 1$. The axial tensor element, in this case, equals $A^{||} = 3.03$ MHz [44]. On the other hand, when we have ^{14}N atom whose nuclear spin is $I = 1$, we will get a separation into three sub levels. The axial tensor element, in this case, is $A^{||} = 2.16$ MHz [45].

1.4 Pulse sequences

As can be inferred from the Hamiltonian (neglecting the hyperfine interaction for this discussion), at zero magnetic field, the $|m_s = +1\rangle$ and $|m_s = -1\rangle$ levels of the NV spin are degenerate. However, when applying a DC magnetic field B_0, Zeeman splitting is induced, and the two levels become separated, enabling us to distinguish between them and deal with a specific transition: $|m_s = 0\rangle \rightarrow |m_s = +1\rangle$ or $|m_s = 0\rangle \rightarrow |m_s = -1\rangle$ each with a specific resonance frequency (when B_0 is large enough we can disregard the other transition because the energy scales become different). Dealing with one of these transitions, we can consider our system as a two-level quantum system (pseudo-spin-$\frac{1}{2}$ subspace) that can serve as a quantum bit ('qubit'). The two orthogonal states of this system represent the classical bits 0 and 1 [46]. The system can be described as a spinor and be expressed as follows

$$|\chi\rangle = \begin{bmatrix} \alpha \\ \beta \end{bmatrix} = \alpha|0\rangle + \beta|1\rangle, \text{ with } |\alpha|^2 + |\beta|^2 = 1 \tag{1.4}$$

A useful way to represent the actions of various operators on a spinor is by the Bloch sphere (see Fig. 1.3). Therefore, it is convenient to use the eigenspinors of $\vec{\sigma} \cdot \hat{n}$, where $\vec{\sigma}$ is the Pauli spin matrices vector, and $\hat{n}$ represents a unit vector along an arbitrary direction. The eigenspinors, in this case, are given by

$$|\xi_n^+\rangle = \cos\frac{\theta}{2}|0\rangle + \sin\frac{\theta}{2}e^{i\phi}|1\rangle \tag{1.5}$$

and

$$|\xi_n^-\rangle = \sin\frac{\theta}{2}|0\rangle - \cos\frac{\theta}{2}e^{i\phi}|1\rangle \tag{1.6}$$

where spherical coordinates are used, and θ is the polar angle while ϕ is the azimuthal angle.

By applying the Ehrenfest theorem, one can calculate the time evolution of the spinor under time-dependent magnetic field $\vec{B}(t)$. The time evolution is governed by the next three coupled equations

$$\begin{aligned} \frac{d}{dt}\langle S_x\rangle &= \frac{g\mu_B}{\hbar}\left(B_y\langle S_z\rangle - B_z\langle S_y\rangle\right) \\ \frac{d}{dt}\langle S_y\rangle &= \frac{g\mu_B}{\hbar}\left(B_z\langle S_x\rangle - B_x\langle S_z\rangle\right) \\ \frac{d}{dt}\langle S_z\rangle &= \frac{g\mu_B}{\hbar}\left(B_x\langle S_y\rangle - B_y\langle S_x\rangle\right) \end{aligned} \tag{1.7}$$

where $\gamma_e = \frac{g\mu_B}{\hbar}$, and g is the electron g-factor while μ_B is the Bohr magneton. These

equations can be reduced to the following convenient representation

$$\frac{d}{dt}\left\langle \vec{S} \right\rangle = \frac{g\mu_B}{\hbar}\vec{B} \times \left\langle \vec{S} \right\rangle = \vec{\Omega} \times \left\langle \vec{S} \right\rangle \tag{1.8}$$

Here, $\left\langle \vec{S} \right\rangle$ is the expected value of the spin angular momentum vector and $\vec{\Omega} = \frac{g\mu_B}{\hbar}\vec{B}$ is the Larmor precession frequency. Actually, at this frequency, the spin angular moment vector $\left\langle \vec{S} \right\rangle$ rotates on a cone which makes a fixed angle with a time-independent magnetic field $\vec{B_z}$. The rotation is described by the azimuthal angle ϕ and is governed by $\frac{d\phi}{dt} = \frac{g\mu_B}{\hbar}B_z$.

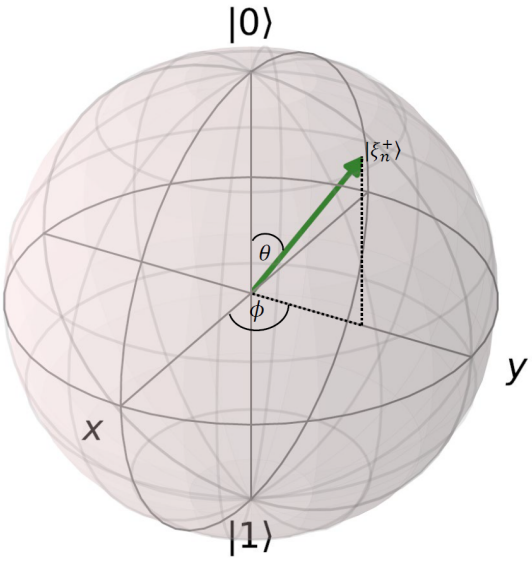

Figure 1.3: Bloch sphere representation [47] including the eigenspinor $|\xi_n^+\rangle$ and the relevant angles defining it.

In our experiments, we wish to manipulate the 'qubit' and flip the spinor. In our case, we initialize the system to the $|m_s = 0\rangle$ state (by a laser pulse, as explained in Sec. 1.2) and want to flip it to the $|m_s = -1\rangle$ state. The combination of magnetic fields required for performing this task includes our constant magnetic field along the z-axis, B_0, and an alternating magnetic field in the x-y plane denoted as B_1. In this case, B_1 has to "chase" the spinor and stay perpendicular to the direction of the spinor ($\hat{n}$) in order to eventually flip it to the other state. Therefore, it is necessary that the frequency of B_1 is equal to the Larmor precession frequency under B_0, which is given by Eq. 1.8 as $\omega_0 = \frac{g\mu_B}{\hbar}B_0$. Moreover, it is needed that the magnitude of this alternating field will remain constant in time. The time it takes the spinor to reach the south pole of the Bloch sphere (flipping) is dependent on the strength of B_1 and is given by $t_{flip} = \frac{\pi}{\omega_1}$, where $\omega_1 = \frac{g\mu_B B_1}{\hbar}$.
An exact calculation of the probability of spin flipping with applying B_0 and B_1 was first performed by *I.I.Rabi* [48] while using the rotating frame method, and is given by

$$P_{0\to1}(t) = |\langle 1|\xi_n^+\rangle|^2 = \sin^2\left(\frac{\theta(t)}{2}\right) = \frac{\omega_1^2}{\omega_1^2 + (\omega_0 - \omega)^2}\sin^2\left(\frac{\sqrt{(\omega-\omega_0)^2 + \omega_1^2}}{2}t\right) \tag{1.9}$$

where ω is the frequency of the driving alternating magnetic field, B_1.
In the rotating frame, the effective magnetic field is given by

$$\vec{B_{eff}} = \left(B_0 + \frac{\omega}{\gamma}\right)\hat{z} + B_1\hat{x} \ . \tag{1.10}$$

When $\omega = \omega_0 = -\gamma B_0$, the effective magnetic field is a constant magnetic field of intensity B_1 along the x-axis. We will have a rotation of a spinor around this axis with an angular frequency ω_1. Thus, assuming a spinor is initialized at the north pole at time $t = 0$, it will reach the south pole at time $t = t_{flip}$, in agreement with the former equations.

The concepts presented here are the key for characterizing the NV system and fitting experimental data to theoretical approximations to infer the flipping rate by which we can eventually generate the MW pulses required to bring us to the state we wish to end at.

1.4.1 Optically Detected Magnetic Resonance (ODMR)

ODMR is a general technique, already applied more than twenty years ago, to investigate the properties of NV centers [49]. By this technique, we can infer the system's resonance frequency. In the measurement, we continuously irradiate the NV while applying continuous MW at different frequencies, as depicted in Fig. 1.4. The laser excitation continuously polarizes the system into the more fluorescent $|m_s = 0\rangle$ ground state, while the MW drives the system into the less fluorescent $|m_s = \pm 1\rangle$ states, once near to resonance. In general, the MW frequency is swept across the NV resonance frequency, enabling the resonance line centers to be determined.

The shot noise limited sensitivity of this measurement is given by [50]

$$\eta_{CW} \approx \frac{4}{3\sqrt{3}} \frac{h}{g\mu_B} \frac{\Delta\nu}{C_{CW}\sqrt{R}} \tag{1.11}$$

where R is the photon detection rate, $\Delta\nu$ is the linewidth, and C_{CW} is the ODMR contrast.

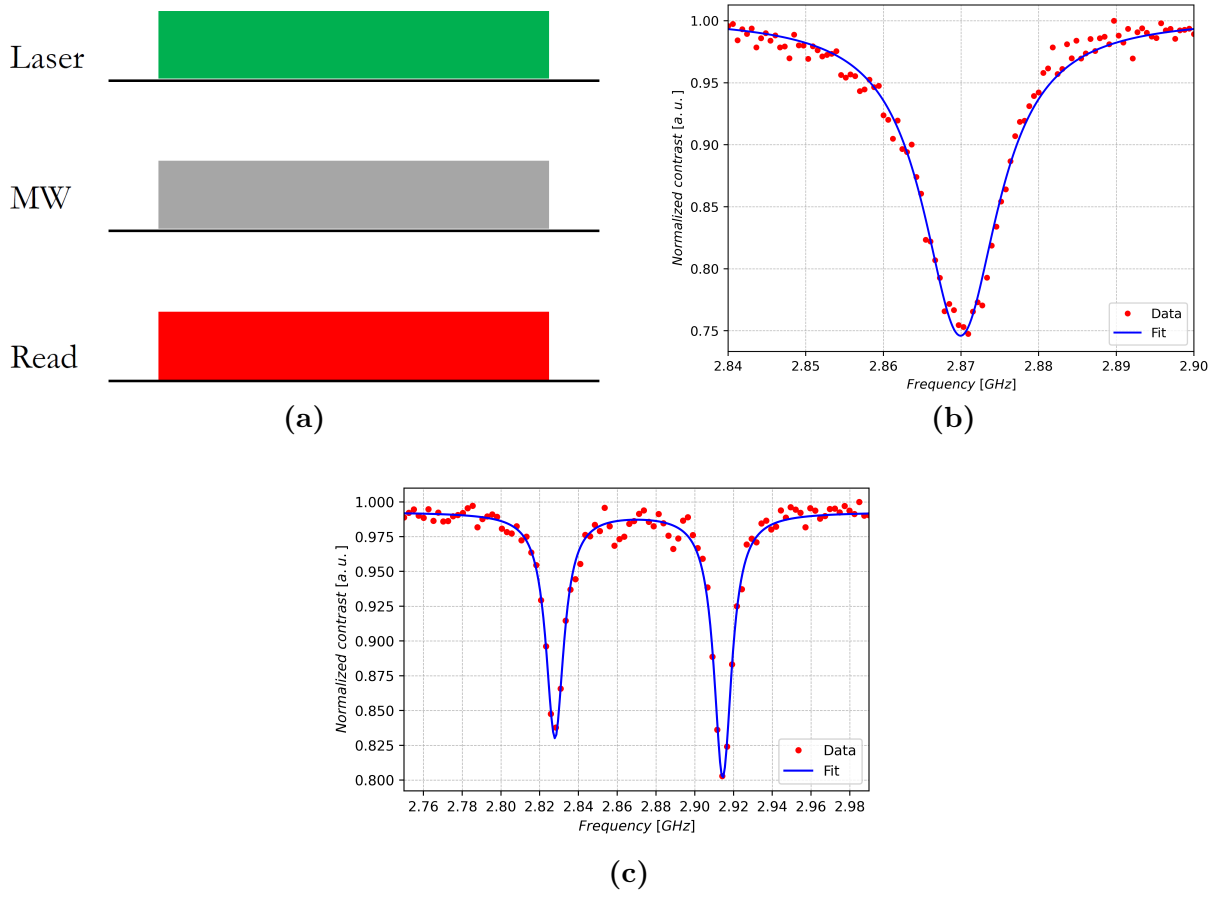

Figure 1.4: ODMR. **(a)** The ODMR pulse sequence. Continuous laser irradiation, MW, and readout are utilized. **(b)** ODMR spectrum at zero magnetic field with a Lorentzian fit [51]. The peak at 2.87 GHz corresponds to the zero-field splitting (ZFS) term (see Eq. 1.1). **(c)** ODMR splitting under DC magnetic field fitted to the sum of two Lorentzian functions. From the separation of the peaks, a magnetic field of $B_0 = 15$ G is inferred.

1.4.2 Pulsed ODMR

The pulsed ODMR magnetometry method was demonstrated thoroughly for NV centers by *Dréau et al* [50]. This technique enables avoiding optical and MW power broadening of the spin resonances, enabling nearly spin dephasing time T_2^*-limited measurements. The ODMR contrast (or ESR contrast) is generally given by

$$\mathcal{C}(T) = \frac{\mathcal{S}(T)}{\mathcal{N}_0(T)} = \frac{\mathcal{N}_0(T) - \mathcal{N}_1(T)}{\mathcal{N}_0(T)} \tag{1.12}$$

where $\mathcal{N}_0(T)$ and $\mathcal{N}_1(T)$ are the total number of collected photons during an interrogation time T for a single NV center prepared in the $|m_s = 0\rangle$ state and the $|m_s = 1\rangle$ state respectively. The effective signal $\mathcal{S}(T)$ saturates when spin populations reach their steady-state values. Therefore, for an interrogation time longer than the metastable state lifetime, the ODMR contrast decreases because the contrast between the $|m_s = 0\rangle$ and the $|m_s = 1\rangle$

states vanishes (derived from Fig. 1.5 which depicts the time-resolved photoluminescence (PL) response of a single NV center).

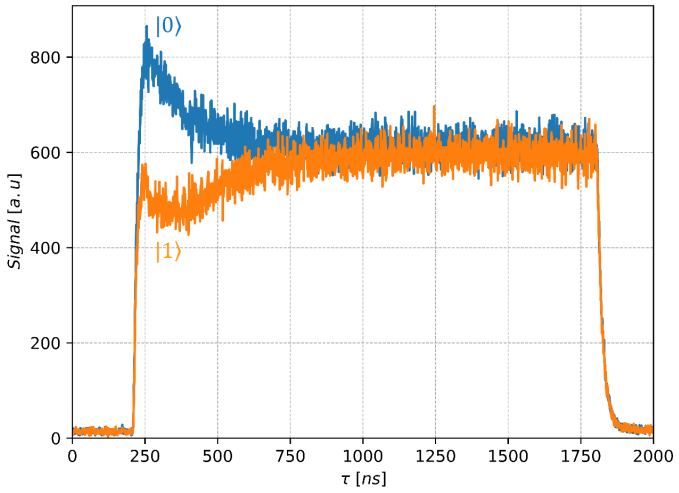

Figure 1.5: Time resolved photoluminescence (PL) response of a single NV center initially prepared in the $|m_s = 0\rangle$ state (blue curve) and in the $|m_s = 1\rangle$ state (orange curve). Preparation in the $|m_s = 0\rangle$ state is performed by a 1.5 µs laser pulse. Initialization in the $|m_s = 1\rangle$ state is achieved by a subsequent MW π pulse. Time binning is 1 ns.

For this reason, one can perform a simple pulsed ODMR sequence in order to overcome this issue. In the pulsed ODMR protocol, depicted schematically in Fig. 1.6a, we first initialize the NV spin state to the $|m_s = 0\rangle$ ground state. Then we apply a MW π pulse at the Rabi frequency, and then the population is read out optically during a second laser pulse. This laser pulse is also used to achieve an efficient preparation of the NV in the $|m_s = 0\rangle$ state for the next MW π pulse. This sequence is repeated many times while looping over different frequencies near-resonance. The pulsed ODMR spectrum linewidth is the Fourier transform of the product of the rectangular-shaped π pulse with a duration T_π and the inhomogeneous Gaussian profile of the NV center spin, characterized by its spin dephasing time T_2^*. This corresponds to a convolution of a sinc function of width T_π^{-1}, with a Gaussian function of width T_2^{*-1}. Assuming the interrogation time is T_2^* we can write the pulsed ODMR linewidth $\Delta\nu$ as $\Delta\nu = \frac{1}{\pi T_2^*}$ (this approximation underestimates the linewidth by a factor of 2 or less). Defining t_I and t_R as the initialization and readout times respectively, the time-averaged photon collection rate R reduces by the readout duty cycle $\frac{t_R}{t_I+T_2^*+t_R}$ [52]. Defining $\mathcal{N} = Rt_R$ to be the mean number of photons collected per optical readout cycle, the pulsed ODMR sensitivity is given by (using Eq. 1.11)

$$\eta_{pulsed} \approx \frac{8}{3\sqrt{3}} \frac{\hbar}{g\mu_B} \frac{1}{C_{pulsed}\sqrt{\mathcal{N}}} \frac{\sqrt{t_I + T_2^* + t_R}}{T_2^*} \tag{1.13}$$

where C_{pulsed} is the pulsed ODMR contrast.

By applying this pulsed ODMR sequence, one can suppress the power broadening of the electron spin resonance (ESR) linewidth, leading to enhancement of the magnetic field sen-

sitivity by roughly one order of magnitude in comparison to CW ODMR (continuous ESR spectroscopy). Moreover, this scheme can also be useful for the study of weak hyperfine interactions of the NV center with nearby nuclear spins [53].

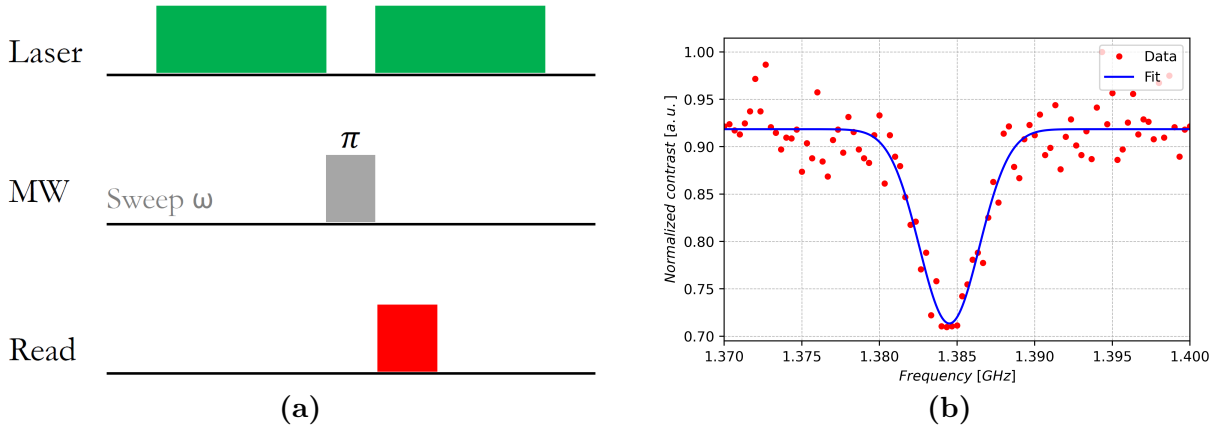

Figure 1.6: Pulsed ODMR. **(a)** The pulsed ODMR sequence decribed in the text. **(b)** Normalized pulsed ODMR spectrum fitted to a Gaussian. The magnetic field is $B = 530$ G.

1.4.3 Rabi Oscillations

As described by Equation 1.10, a resonant magnetic field B_1 brings to a rotation of the electron spin around the x-axis of the rotating frame. Thus, the spin population will continuously change while applying a MW frequency of $\omega = \gamma B_0$, as described by Eq. 1.9. The Rabi measurement is similar to the pulsed ODMR sequence except for the fact that here the frequency is fixed, and the pulse duration is varied as described in Fig. 1.7a. The laser pulse is used to perform a measurement of the electron spin state, which can be seen as a projection of the electron spin on the z-axis of the NV (the spin quantization axis). By applying the sequence, we can infer the time for a rotation into the balanced superposition state ($\frac{\pi}{2}$ time) as well as the time for full spin inversion (π time) (For instance, 90 ns and 180 ns respectively in Fig. 1.7b). Hence, this measurement and the ODMR measurement are crucial prerequisites for defined MW pulses to perform precise spin manipulations.

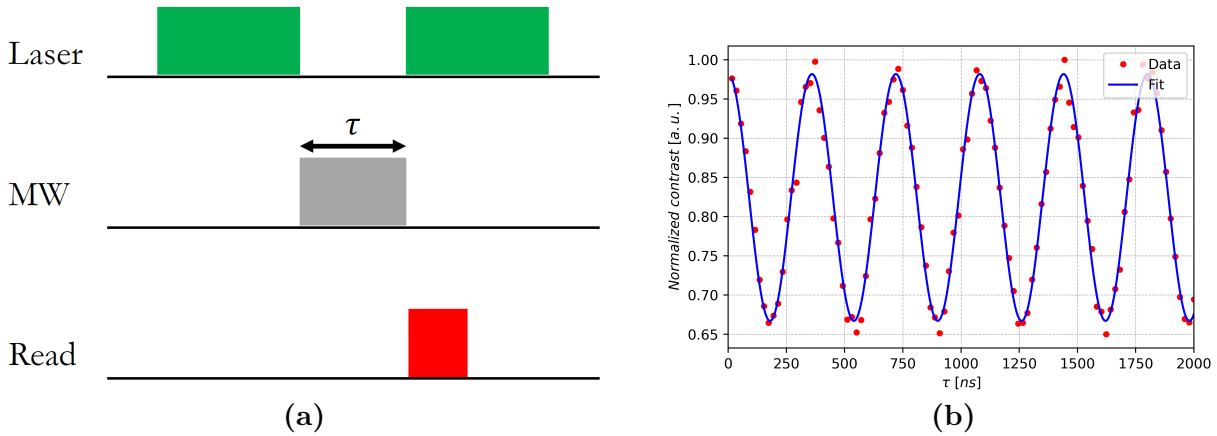

Figure 1.7: Rabi oscillations. **(a)** The Rabi oscillation sequence. **(b)** Normalized Rabi oscillation spectrum with a decaying cosine fit ($A \cdot e^{-\frac{\tau}{T}} \cos(\Omega\tau) + c$).

1.4.4 Ramsey Interferometry

In this method, DC magnetic fields can be sensed. In the Ramsey technique, which is also called free induction decay (FID), the spin state is first initialized to the $|m_s = 0\rangle$ state. A resonant magnetic field B_1 is applied for a particular finite duration of $\frac{\pi}{2\omega_1}$ (defined after applying the discussed Rabi sequence), which is also known as a $\frac{\pi}{2}$ pulse, which brings the initial state into a balanced superposition of the two eigenstates $|m_s = 0\rangle$ and $|m_s = +1\rangle$, given by

$$|\Psi\rangle = \frac{1}{\sqrt{2}} (|0\rangle + |1\rangle) \tag{1.14}$$

This state is then left to precess freely for a duration τ (evolution time) without any perturbation. During this time, the NV spin interacts with the external magnetic field,

and a magnetic field-dependent phase φ is accumulated between the two states. This phase corresponds to a precession of the spin in the plane perpendicular to the spin quantization axis z, giving the state

$$|\Psi\rangle = \frac{1}{\sqrt{2}}\left(|0\rangle + e^{i\varphi}|1\rangle\right) \tag{1.15}$$

where the phase φ is given by

$$\varphi = \int_0^\tau \gamma_e B_z dt = \int_0^\tau \gamma_e \Delta_{DC} dt \tag{1.16}$$

Later on in the sequence, this phase is measured by applying a second $\frac{\pi}{2}$ pulse, which gives the projection of the NV spin state back onto the quantization axis (pulse sequence described in Figure 1.8a). Therefore, the phase is converted into probabilities that are read out optically through the spin-dependent fluorescence of the NV center. By increasing the free evolution time τ, the magnetic sensitivity can be improved. However, this evolution time τ is limited, and we reach a decrease in the spin readout contrast while it increases. This phenomenon is due to magnetic field noise from the environment of the NV, which randomizes the phase φ over time with a time constant which is the spin dephasing time, T_2^*. The measurement plotted in Figure 1.8b shows an FID measurement where two effects can be noticed. First, one can notice the exponential decay, which is governed by the characteristic dephasing time T_2^*. Second, one can notice the oscillation, which is derived from detuning of 1.8 MHz from the resonance frequency as inferred from performing Fast Fourier Transform (FFT) analysis (Figure 1.8c). This is equivalent to having a detuned magnetic field Δ_{DC}, such that, as explained by Eq. 1.15 and Eq. 1.16, we get oscillations due to precession in the rotating frame of the system. Overall, the signal as a function of the evolution time is given by

$$S(\tau) = exp\left[-\left(\frac{\tau}{T_2^*}\right)^2\right] A_i \cos(2\pi\Delta_i\tau + \phi_i) + c_{bias} \tag{1.17}$$

where Δ_i is the detuning, A_i is the amplitude, and ϕ_i is the relative phase.

Comparing the loss in readout contrast to the gain in the increased acquired phase, it was shown that the magnetic field sensitivity is optimized when $\tau = T_2^*$ [54]. The magnetic field sensitivity obtained when using an optimized evolution time is given by [28]

$$\eta \approx \frac{\hbar}{g\mu_B} \frac{1}{C\sqrt{\mathcal{I}_0 t_L}} \frac{1}{T_2^*} \tag{1.18}$$

where $\mathcal{I}_0$ is the NV center fluorescence rate, and t_L is the readout laser pulse duration.

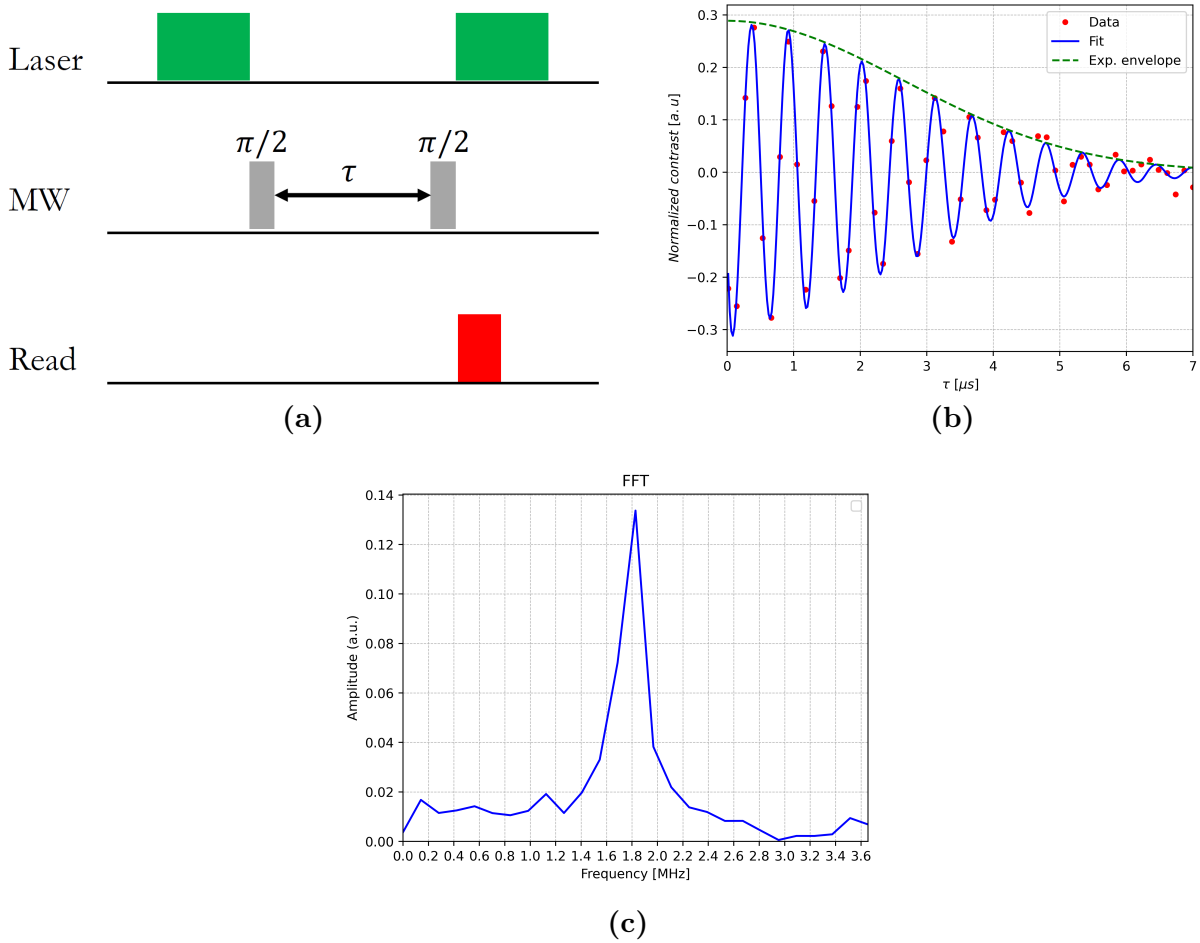

Figure 1.8: Ramsey Interferometry. **(a)** The pulse sequence for a Ramsey measurement. Two MW $\pi/2$ pulses are applied separated by varied evolution time τ. The first MW pulse brings the spin to the balanced superposition state, where it acquires a phase during the free evolution time. The second MW pulse projects the state to the quantization axis. **(b)** The normalized contrast (red dots) shows an exponential decay and oscillation due to frequency detuning. A fit (in blue) was performed using Eq. 1.17 where the exponential envelope (in green) is shown. In this case $T_2^* \approx 3.7$ µs. **(c)** FFT analysis for the measurement shown in (b). A detuning of 1.8 MHz is inferred.

1.4.5 Spin Echo (Hahn Echo)

The spin-echo is basically a modified Ramsey sequence. The remarkable discovery of spin echoes was made by *Erwin Hahn* [55]. This discovery brought to the development of various pulse methods in NMR and is considered among the most significant contributions to magnetic resonance [56]. In the spin-echo sequence, a MW π pulse is given in the middle of the Ramsey sequence, between the two $\pi/2$ pulses as explained in Figure 1.9a. In this method, the first $\pi/2$ pulse has the same effect as in the Ramsey sequence, where the spin is brought from the initial state into a balanced superposition of the two eigenstates $|m_s = 0\rangle$ and $|m_s = +1\rangle$ as explained by Eq. 1.14. This state is then left to precess freely for a duration τ without any perturbation. During this time, the NV spin interacts with

the external magnetic field, and a phase φ is acquired between the two states (Eq. 1.15). After this stage a MW π pulse is given (with the same phase so that B_1 lies again in the $+x$ direction of the rotating frame which is an important requirement for Hahn echo pulses), which swaps the phase acquired between the two states $|m_s = 0\rangle$ and $|m_s = +1\rangle$, namely performing the following operation $|\Psi\rangle_{\pi^-} = \frac{1}{\sqrt{2}}(|0\rangle + e^{i\varphi}|1\rangle) \rightarrow |\Psi\rangle_{\pi^+} = \frac{1}{\sqrt{2}}(e^{i\varphi}|0\rangle + |1\rangle)$ where the first spinor describes the state right before the π pulse, and the second spinor describes the state achieved right after the π pulse (this can be understood by using the Bloch sphere representation of the rotating frame). Thus, in the next free evolution time τ, which is equal to the first one, this phase will ultimately be canceled. Later on, another $\pi/2$ pulse is applied in order to project the spin state into the system axis of quantization (the z-axis). This pulse sequence increases the NV spin coherence by dynamical decoupling of the NV from its environment. Dephasing processes due to random noise are reduced, and the spin coherence time is modified to T_2, the spin-echo decay time or the decoherence time. An example for a Hahn echo measurement can be seen in Figure 1.9b, where the signal is fitted with a Gaussian function of the form [57, 58]

$$S(\tau) = A \cdot exp\left[-\left(\frac{\tau}{T_2}\right)^p\right] + c_{bias} \tag{1.19}$$

Here, A is the amplitude, T_2 is the characteristic decoherence time, and c_{bias} is the offset.

By using such a decoupling sequence, the NV's AC magnetic field sensitivity is improved in comparison to the DC sensitivity as follows

$$\eta_{AC} = \eta_{DC}\sqrt{\frac{T_2^*}{T_2}} \tag{1.20}$$

However, the bandwidth is reduced, and therefore the NV becomes insensitive to frequencies in the order of $\lesssim 1/T_2$.

A prominent effect that can be detected with the Hahn echo sequence is the signal that stems from ^{13}C, which can be located nearby the NV center (1.1% abundance) [59]. In this case, we will observe collapses and revivals of the signal derived from the Larmor precession of the carbon spin (see Figure 1.9c). The Hahn echo sequence in this case has a central filter frequency of $\frac{1}{2\tau}$, so that when $\tau = n \cdot \frac{1}{2 \cdot f_{^{13}\mathrm{C}}^{Larmor}}$ where n is an odd number, we get collapses. At this specific τ_n, the phase accumulation is maximized, so this is where we get the minimal signal.

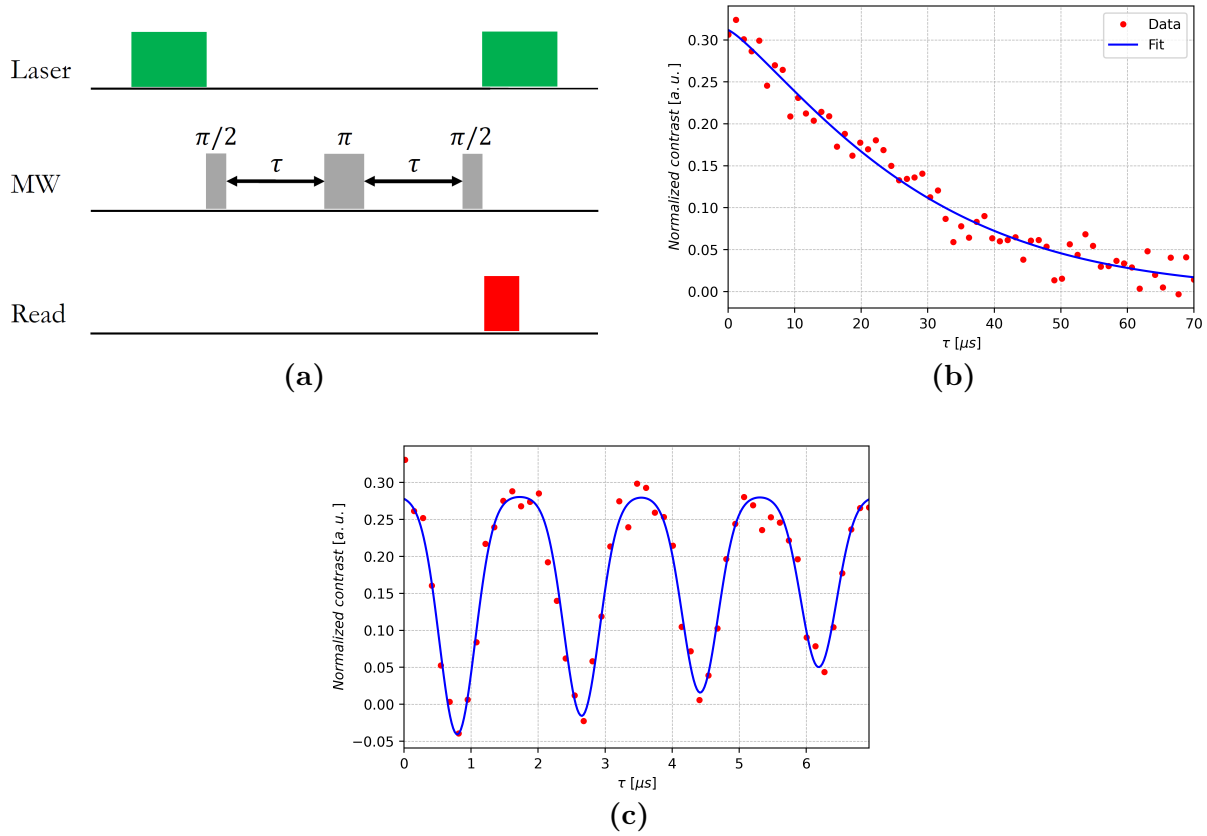

Figure 1.9: Spin Echo. **(a)** The pulse sequence of a Hahn echo measurement. Two MW $\pi/2$ pulses and a MW π pulse in between them are applied, separated by varied evolution time τ from each other. The first MW $\pi/2$ pulse brings the spin to the balanced superposition state, where it acquires a phase during the free evolution time. Then, after an evolution time τ, a π pulse is applied which swap the phase acquired between the two states $|m_s = 0\rangle$ and $|m_s = +1\rangle$. After another evolution time of τ, the phase acquired is ultimately canceled. Later on, another $\pi/2$ pulse is applied in order to project the spin state into the system's axis of quantization (the z-axis). This pulse sequence enhances the NV spin coherence by dynamical decoupling of the NV from its environment. **(b)** Hahn echo signal. One can observe the exponential decay, which can be attributed to spin dephasing induced by random noise. The function is fitted with Eq. 1.19, where the extracted parameters are $p = 1.2 \pm 0.2$, and $T_2 = 29 \pm 2$ µs. **(c)** Hahn echo signal where we have nearby ^{13}C. The observed collapses and revivals of the signal derive from the Larmor precession of the carbon nuclear spin. We get collapses at odd multiplicities of $\tau_{f_{^{13}\mathrm{C}}} = \frac{1}{2 \cdot f_{^{13}\mathrm{C}}}$ and revivals at even multiplicities of τ as expected. (In the measurement conditions $f_{^{13}\mathrm{C}} = \gamma_{^{13}\mathrm{C}} \cdot B = 0.5755$ MHz where $B = 537$ G).

1.4.6 Double Electron-Electron Resonance (DEER)

A pulse sequence applied for detecting nearby spin systems is the Double Electron-Electron Resonance (DEER) sequence which is a modified Hahn echo sequence. During the π (π_{NV}) pulse given for the NV spin, we also apply a π (π_D) pulse for an external nearby spin (also known as a "dark spin", where in our case the dark spin is a spin-label). The sequence used in this thesis (see Figure 1.10a) is a variation of the protocol used in Ref. [7] and is described in Ref. [8]. Except for the π_D pulses, the rest of the sequence is the same as explained in the previous section (Sec. 1.4.5). This technique of applying a second π_D pulses cancels the decoupling of the NV spin to the dark spin and enables the detection of the dark

spins by being sensitive to magnetic field changes during one of the free evolution times τ in which the pulse was applied. The first π_D pulse applied is not essential when dealing with high-frequency pulses used for electron spins; however, it reduces noise and enhances the measurement contrast. Thus, two identical π_D pulses with the same length as the π_{NV} pulse were applied in each half of the sequence. During the measurement, one fixes on a specific evolution time τ determined based on the Hahn echo measurement (choosing τ which is relatively long but that also gives a reasonable signal contrast), and the frequency is swept across the predicted resonance frequency of the dark spin, f_D (based on the measured magnetic field B_0). When the MW frequency hits the right frequency of the π_D pulse, the longitudinal magnetization of the dark spins will be flipped, creating a dipolar magnetic field that is reversed in synchrony with the Hahn echo sequence applied to the NV center. This synchronous reversal will disrupt the spin-echo response, as can be seen in Figure 1.10b.

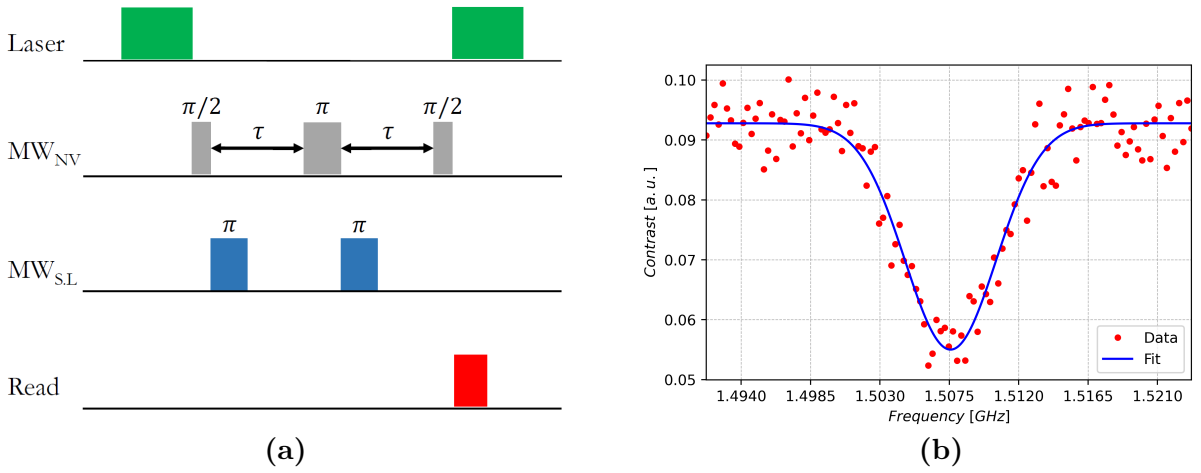

Figure 1.10: DEER. **(a)** The pulse sequence of a DEER measurement described in the text. **(b)** DEER signal arises from nitroxide spin-labels fitted with a Gaussian function [51]. The magnetic field is $B = 537$ G.

2 Experimental Setup

2.1 Room temperature magnetometer setup

The NV center can be utilized as a magnetometer with a frequency bandwidth ranging from DC to GHz and magnetic fields from zero-field to several Tesla [60, 61]. The NV center is confined to a specific single site in the lattice structure, and the magnetic detection volume is in the scale of nanometers. As such, it can be used as a point sensor to sample magnetic fields and possibly image tiny magnetic structures [10]. To extend the magnetometer to a two-dimensional imaging sensor, a piezoelectric stage is used to allow rastering of the sample relative to the laser spot. The sample is optically accessed from below. A permanent magnet is mounted on a motorized stage and is used to apply DC magnetic fields to the NV center. A thin copper wire on top of the NV and close to it is used to apply the MW field for executing spin manipulations.

2.2 Confocal microscopy with nitrogen-vacancy centers

A confocal microscope is used for the optical polarization and readout of the NV center (Fig. 2.1, system built by *Inbar Zohar*). By using a green light laser at a wavelength of 520 nm, optical excitation is performed. The laser light is generated by a laser diode (DLnsec, LABS electronics). The green laser beam passes through a band-pass filter (FBH520-10, FWHM=10 nm) to enhance the isolation of the 520 nm laser line. Then, the green laser beam is guided through a single-mode fiber (SMF) to ensure a Gaussian beam profile. Afterward, the beam is deflected towards the sample stage via a short-pass dichroic beam splitter (DMSP567). The laser beam is focused onto the sample via an objective lens (MPLFLN 100x, NA = 0.9). The objective is mounted beneath a nanometer resolution XYZ piezo stage (TRITOR® 102) with a traveling range of up to 100 µm in all three axes. By scanning the stage, the laser focus is scanned across the sample, and confocal images can be recorded.

The objective is collimating red fluorescence light emitted by the NV center onto the same optical path as the excitation laser beam. After it passes the dichroic beam splitter (DMSP567), the red light is focused onto the center of a 50 µm pinhole by a lens. A second lens is focusing the beam onto two avalanche photodiodes (APD) via a 50:50 beam splitter. This configuration is also known as a *Hanbury-Brown and Twiss* setup [62] which allows recording auto-correlation functions of detected photons. Residual laser light is filtered out by a 731 nm band-pass filter (FF01-731/137-25).

2.3 Microwave radiation

The experiments performed in this thesis required sequences of MW pulses at different frequencies. The electron spins were manipulated by MW fields with frequencies between 1.2-

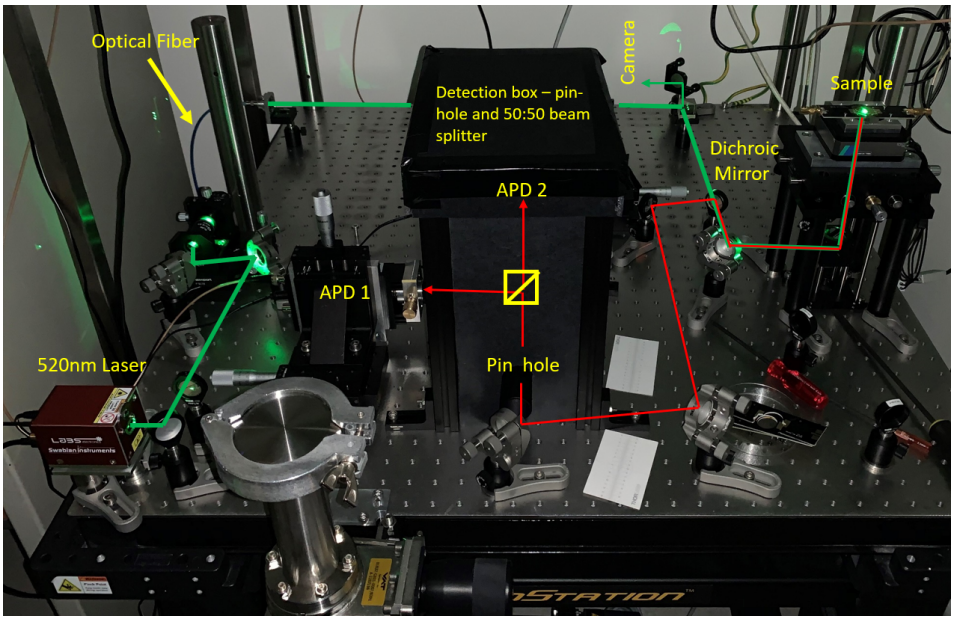

Figure 2.1: The optical setup with all the relevant components discussed in the work.

1.6 GHz. A continuous MW signal was generated using an RF signal generator (SynthNV PRO, Windfreak Technologies, LLC). An IQ mixer (in-phase and quadrature components, Marki IQ-1545LMP) was used to modulate the signal via single/double sideband mixing. In this way, we achieved a pulsed signal whose frequency, phase, and amplitude could be controlled. The I- and Q- input signals were generated by using the Operator-X (OPX) instrument (QUANTUM MACHINES). The signal is later amplified by a custom-made amplifier (ELITE RF, 20 - 6000 MHz, 15 W). The detection of external electron spins requires active manipulation of the sensed electron spins at frequencies between 1-2 GHz. In this case, the magnetic field is ∼500 G, such that the frequency is similar to the resonance frequency of the NV center's electron spin, and both signals can be executed through the same apparatus. The signal passes through a copper wire located on top of the diamond and as part of the PCB, to which the diamond is glued. A scheme for this is depicted in Fig. 2.2.

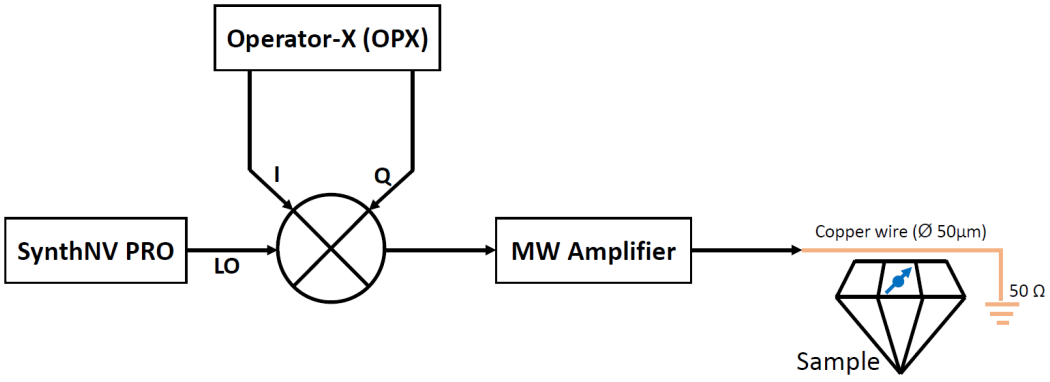

Figure 2.2: The setup for generating MW pulses for spin manipulation and sensing of external spins.

3 EPR Spectroscopy of the Spin Labels

3.1 Sample preparation

3.1.1 Spin labeling of poly-L-lysine

18.8 mg of the poly-L-lysine (P7890-25MG, Sigma-Aldrich), which has a molecular weight ranging from 15,000 - 30,000 (g/mol), were dissolved in a 10 ml solution of phosphate-buffered saline (PBS) to obtain a concentration of 2 mg/ml. Beforehand, a solution of the spin label, 1-oxyl-2,2,5,5-tetramethylpyrroline-3-carboxylate NHS ester (OXYL-1-NHS) (16148, Cayman Chemical) was prepared, with a concentration of 0.5 mg/ml in dimethyl sulfoxide. 500 µl from this solution were added to 500 µl of the Poly-L-lysine (PLL) solution for the labeling reaction to take place (Fig. 3.1a). The quantities were chosen such that ∼15% of the lysines in the solution would be labeled (every structure unit of the PLL can hypothetically be labeled). The mixture was incubated for 1 hour at RT under rotation. Afterward, the mixture was incubated under rotation overnight at 4 ^{0}C . To remove residual by-products of the labeling process and remainders of the unreacted spin label, the solution was dialyzed using a GeBAflex tube (MWCO = 8000, GeBA). A PD-10 column (GE Healthcare) was used to improve the cleaning process, and the first fraction of the solution, mainly containing the labeled PLL, was eluted.
In Fig. 3.1b, the CW EPR measurement for the synthesized material can be seen. It can be inferred that the labeling process succeeded to some extent based on the differences in the height of the right hyperfine peak of the species (For the PLL+SL graph in red, the peak is lower than for the SL itself, in blue), which is dependent on the tumbling rate [10, 63]. A slow tumbling process can be inferred from the lower height of the right hyperfine peak, which is a sign of successful attachment of the spin label OXYL-1-NHS to the amine sites of the Poly-L-lysines.

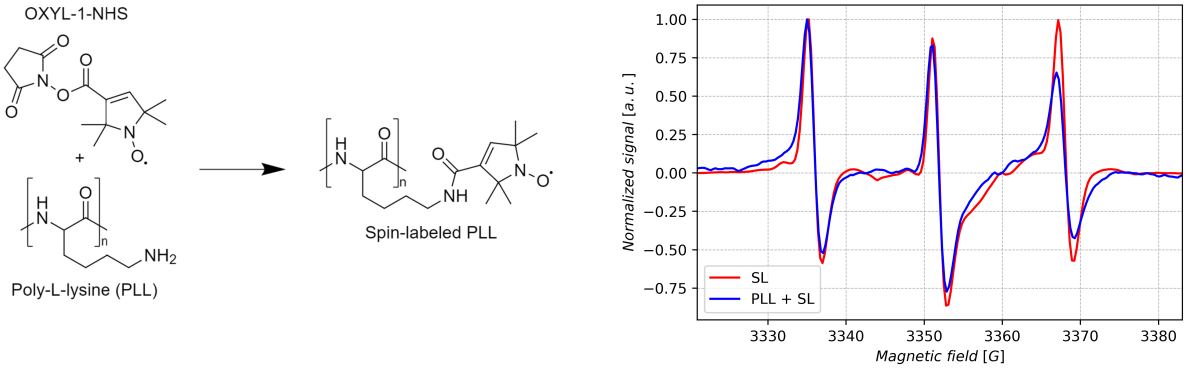

(a) **(b)**

Figure 3.1: **(a)** The spin labeling reaction performed on poly-L-lysine (PLL) with nitroxide spin labels (OXYL-1-NHS). The creation is escorted by the formation of an amide bond which is pretty stable [64]. **(b)** Room temperature X-band EPR measurement (ν = 9.423 GHz) performed for the labeled PLL (in blue) and the spin label itself (in red). One can observe that the third peak is smaller for the labeled PLL, which is a good indication for the labeling process [10, 63].

3.1.2 Diamond sample preparation

For the experiments presented in this chapter, shallow NV centers in a diamond membrane (30 µm thick) were used. These NV centers were created by nitrogen ion implantation with an energy of ∼5 keV, corresponding to an averaged depth of ∼8 nm. Later on, using lithography techniques, nanopillars were fabricated. These nanostructures enhance the photon collection efficiency of the NV centers because they act as waveguides [65]. A considerable number of the nanopillars contained a single NV, enabling to perform experiments. Initially, the diamonds were cleaned for two hours by an acid-boiling procedure [7] which also activates the NVs to their negatively charged state. In this procedure, equal amounts of nitric acid (HNO_3), sulfuric acid (H_2SO_4), and perchloric acid ($HClO_4$) are used, and the cleaning process performs at the boiling point of the mixture. Later on, the spin labeled PLL was placed at the surface of the diamond using a thin copper wire (≈ 50 µm). The copper wire was dipped inside the spin labeled PLL solution, and then the liquid was drop cast when positioning the wire close to the diamond surface. This technique was found to be much more accurate than the conventional method of using a pipette with a small volume of 0.2 µl, that gave a big radii spread drops where it was difficult to position the spot accurately. By using a microscope and detecting the coordinates of the grids, the predefined position to drop cast was determined. Fig. 3.2a shows the diamond sample attached to the PCB with the copper wire on top, while Fig. 3.2b shows a magnified image of the diamond sample during the drop-casting process. One can observe that a tiny drop was achieved.

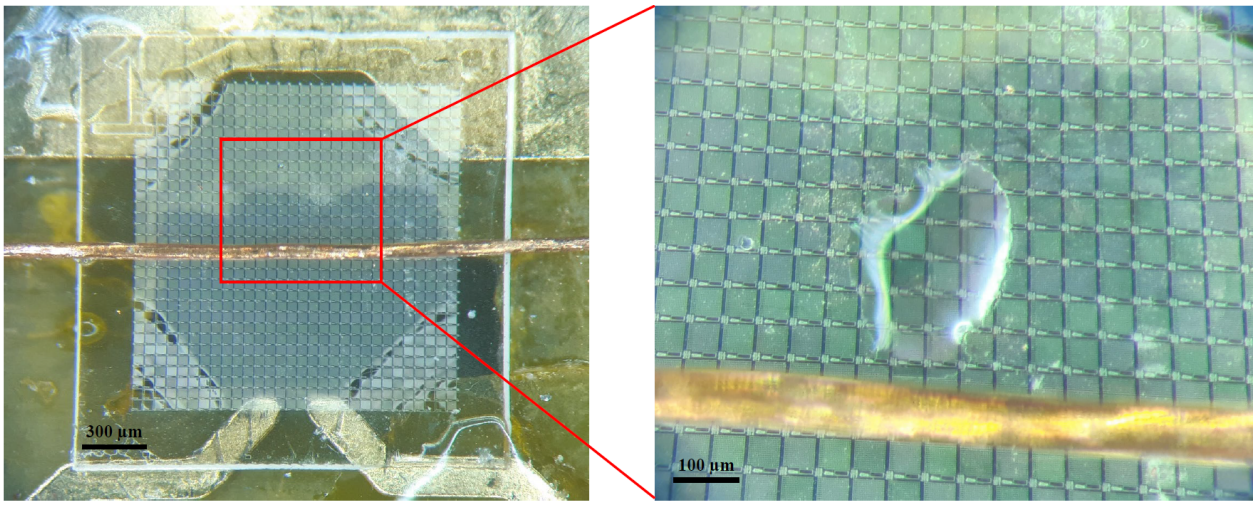

Figure 3.2: The diamond sample. **(a)** The diamond sample connected to the PCB via two pieces of wax at its corners (CRYSTALBOND 509). One can observe the grids and the copper wire used for generating the AC magnetic field, B_1. **(b)** Magnified image of (a), after performing the drop-casting process, at the accurate position where the liquid was drop cast by using a thin copper wire.

3.2 Nanoscale EPR experiments

3.2.1 Applying the DEER sequence

In order to detect the external spins, the DEER sequence was applied. First, we tried to detect the labeled PLL; however, many challenges arose during the experiments. There were software issues and instrumentation issues that hindered the possibility of getting a signal considering that such a measurement has not been performed beforehand in the current setup. Therefore, we decided to first try and measure a signal due to the spin label itself (OXYL-1-NHS) because, in this case, we have a larger concentration of spins, and it should be easier to get a signal. In this way, it also isolated this issue and made us confident it would not be the source for unsuccessful measurements.

As explained in section 1.4.6, we can specifically couple the NV spin to the spin label by the discussed DEER sequence. The configuration of the pulse effectively decouples the NV spin from off-resonance magnetic fields while enhancing the effect caused by the resonant magnetic field, i.e., increasing the phase accumulation in this case. Because the decoupling frequency of sequences such as the Hahn echo sequence discussed in section 1.4.5 or other sequences such as CPMG (Carr-Purcell-Meiboom-Gill pulse sequence) [66] or XY4 [67, 68], is limited to a few MHz, the Larmor precession of electron spins (GHz range) can not be detected directly. Thus, a second MW pulse manipulates the nearby electron spin to invert its direction in sync with the NV spin. This process modulates the magnetic field generated by the nearby spin into an AC magnetic field with a frequency determined by the sequence. By sweeping the MW frequency, measurements of the target spin can be executed. In this work, the sequence which was used in order to perform NV center-based

DEER spectroscopy is described in Figure 1.10a. As explained, the two spin species in the sequence are controlled individually due to their different resonance frequencies, which enable to perform the measurement. The measurements were performed at frequencies near the intersection between the NV $|m_s = -1\rangle$ state's resonance frequency and the electron spin resonance frequency (see Fig. 3.3). Thus, working at magnetic fields of 400-600 G and frequencies around 1.5 GHz.

A benefit from working at this magnetic fields is the proximity to the excited-state level anticrossing (ESLAC). Near the ESLAC, electron spin polarization is effectively transferred to the nuclei, achieving a nearly complete ^{15}N polarization under a wide range of magnetic fields [69, 70]. In this case, we have one resonance frequency for the NV instead of several, which makes the DEER measurement more accurate and prevents the emergence of misleading signals of other possible resonances arising from the hyperfine coupling (the hyperfine coupling term is described by Eq. 1.2 and Eq. 1.3).

In the experiments, the π pulse for the target spin was applied immediately after the π pulse for the NV spin and not simultaneously (which is ideal) because only one amplifier was used. However, because the evolution times (τ) were much larger than the pulses lengths (at least by 20), the sequence is still valid.

As was discussed in the introduction, DEER spectroscopy via NV centers was already performed successfully for the detection of several electronic species such as nitrogen defects [5, 6], radicals [8], NV centers [8], and spin labeled proteins [9, 10]. A prerequisite for the technique is that the random spin flips of the target spins will have a time scale that is longer than the sequence duration. Therefore, the longitudinal relaxation time T_1 of the target spins should be greater than the total measurement time, i.e., $T_1^{SL} > 2\tau$.

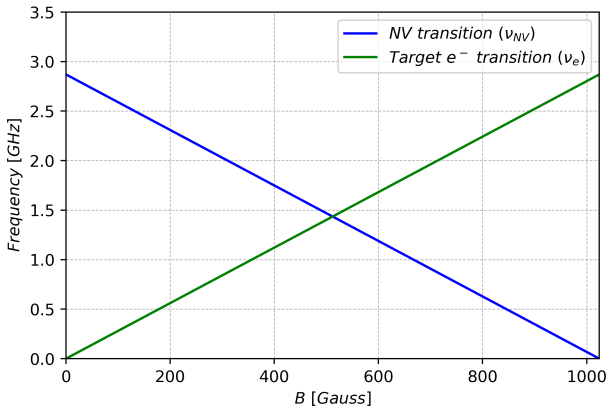

Figure 3.3: Resonance Frequencies. The NV resonance frequency as a function of B_0 (in blue) with accordance to the simple linear equation $f_{NV} = D - \gamma_e B_0$ (based on the simplified Hamiltonian). This transition is from the $|m_s = 0\rangle$ state into the $|m_s = -1\rangle$ state. The assumed target electron resonance frequency (in green) as a function of B_0 where $f_e = \gamma_e B_0$. The experiments in this work were performed at magnetic fields between 400 G to 600 G, that are around the intersection point (512 G).

3.2.2 ESR for nitroxide spin labels via NV centers

The SL has an electron spin of $\frac{1}{2}$ and a nuclear spin of 1 due to the ^{14}N of the nitroxide group. Thus, the Hamiltonian of the investigated SL is given by

$$\hat{\mathcal{H}}_{SL} = \gamma_e B \cdot \hat{\sigma} + \hat{\sigma} \cdot A \cdot \hat{I} \tag{3.1}$$

where $\hat{\sigma}$ is the spin operator of the SL electron spin and A is the hyperfine tensor. Assuming the DC magnetic field is aligned along the NV center's axis, the hyperfine tensor has the next diagonal form (in the SL coordinate system)

$$A = \begin{pmatrix} A_{xx} & 0 & 0 \\ 0 & A_{yy} & 0 \\ 0 & 0 & A_{zz} \end{pmatrix} \tag{3.2}$$

where $A_{xx} = A_{yy} = 14$ MHz and $A_{zz} = 103.2$ MHz. Therefore, the SL should have three transition frequencies which are dependent on the tilt angle between the SL and the NV axis. This hyperfine structure of the spin label can be detected by the NV center, resembling a "nano EPR instrument". However, in the following, the hyperfine splitting was not observed, probably due to the power broadening of the signal and the number of nearby spin labels. Detection of considerable number of spins might result in spin exchange effects which wash out the hyperfine structure [51]. Moreover, the measurements were performed at RT, not at low temperatures, with cryogenic systems where the obtained DEER signal is almost not influenced by the movement of molecules, and the molecules are much more protected from photobleaching processes.

DEER signals were obtained after applying the NHS radical (OXYL-1-NHS) to the diamond surface and after cleaning it with acids (acid boiling, see Sec. 3.1.2). The DEER signal was obtained from 3 different NVs for each case. The two measured spectra obtained from one of the NVs (NV1) are shown in Fig. 3.4. In this Figure depicted are the signals before and after cleaning the diamond surface to which the SL was applied. Ideally, it would have been better to obtain a DEER signal before applying the radical. However, some of the NVs that were pre-characterized did not yield results, and some were quenched after applying the material, probably due to the interactions with the SLs. There were also several NVs that went through charge state conversion from the desired negatively charged state (NV^-) into the undesired neutral state (NV^0), which does not exhibit the appealing optical and spin properties of the former state [71–73]. Moreover, because the applied material was fluorescent, it was challenging to find the pre-characterized NVs in the setup. Thus, the presented results were obtained from NVs that were characterized only after applying the SL to the diamond surface.

From the DEER spectra obtained for NV1, we can deduce that the signal originated from

the SLs and not from other possible electronic species described in Sec. 3.2.1.

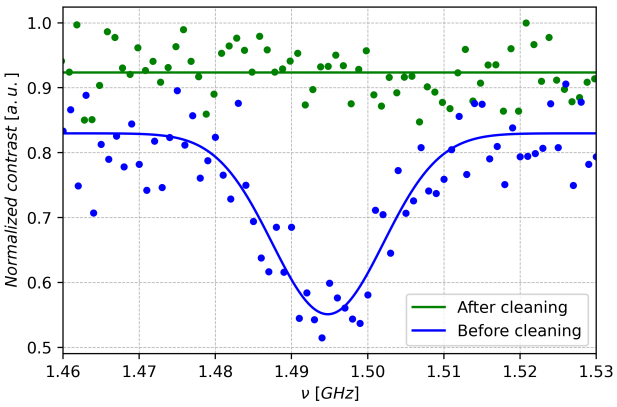

Figure 3.4: DEER measurement (NV1). DEER spectra obtained before (in blue) and after (in green) cleaning the diamond with the NHS spin label. A single peak is observed when applying the material, and after cleaning the surface with acids, no peak is detected to get a flat line. The peak in blue is fitted to a Gaussian function (FWHM $= 17 \pm 2$ MHz). The magnetic field in the measurement is $B = 532$ G.

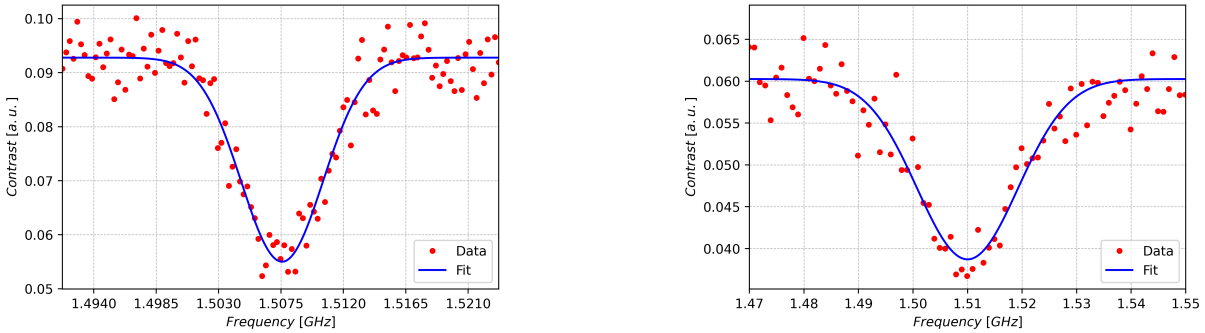

Figure 3.5: Additional DEER spectra obtained from different NVs: **(a)** NV2, and **(b)** NV3. The signals are fitted to a Gaussian function and originate from several spin labels. The magnetic field in both cases is ≈ 537 G. For NV2, FWHM $= 6.8 \pm 0.2$ MHz and for NV3, FWHM $= 22 \pm 1$ MHz.

Fig. 3.5 depicts the DEER spectra obtained from the other two NVs (NV2 and NV3). For NV2, the full width at half maximum (FWHM) is 3 times narrower than the FWHM of NV3. This might result from detecting a smaller number of spins such that the distribution is more centered. Moreover, although the theoretical applied MW power is the same (5 dBm), due to geometrical reasons (distance between the NV and the copper wire as well as the angle between them) the π pulse time for NV2 is 114 ns and for NV3 is 105 ns. Therefore, we can deduce that the power applied on NV3 is larger and might bring to power broadening [50]. Thus, these three hypotheses might explain the obtained differences in the structure of the curves. On the other hand, the difference in the contrast for each measurement is derived from the different chosen evolution times and the corresponding decoherence time of each NV. The evolution time in the measurement of NV2 is 4 times shorter than the evolution time used for NV3 (4000 ns in comparison to 1000 ns). The decoherence time (T_2) of NV2

is ~ 1 µs, and the decoherence time of NV3 is ~ 4 µs. Thus, under these circumstances, the maximal possible contrast of NV2 is higher than that of NV3, 0.1 and 0.065, respectively. (The magnetic field is 537 G in both measurements, and the NVs' orientation is identical).

For NV3 (b), the signal obtained after cleaning the surface was not prominent but noisy. However, it is still possible to deduce that the signal derives from the SL based on the structure of the graph, which can be achieved without the need for many measurement repetitions and in spite of the fact that the graph is noisy. For NV2 (a), after cleaning the surface, a small peak in the DEER signal was obtained probably due to unsuccessful cleaning of the whole surface, which could be noticed in the confocal scan (fluorescent residues were left).

All the graphs were fitted with Gaussian functions based on the assumption that the signal is composed of many Lorentzian functions due to a large number of nearby spins with different orientations, where we assume a normal distribution [51]. The minimum concentration of spin labels (before the evaporation of the solvent) is 7 molecules per 1 nm^3, which leads to a Gaussian spread of the Lorentzian functions. Currently, we try to understand whether it is possible to extract more conservative estimation of the spin labels density, but this is beyond the scope of this thesis.

3.2.3 Effect of laser irradiation

During the measurements, a decay of the fluorescence over time was observed, as depicted in Fig. 3.6, and signals were also found to vanish. In Fig. 3.6a, one can observe the confocal image obtained before prolonged irradiation (the bright clusters are the spin labels). In Fig. 3.6b, one can observe the confocal image obtained at the same position after prolonged laser irradiation at several spots. Some of the spots, where the change was prominent, are marked with red circles. Here, we can see that fluorescence decreased and also vanished at some points. This effect was also investigated by NV-based EPR spectroscopy by utilizing the DEER sequence on several NVs.

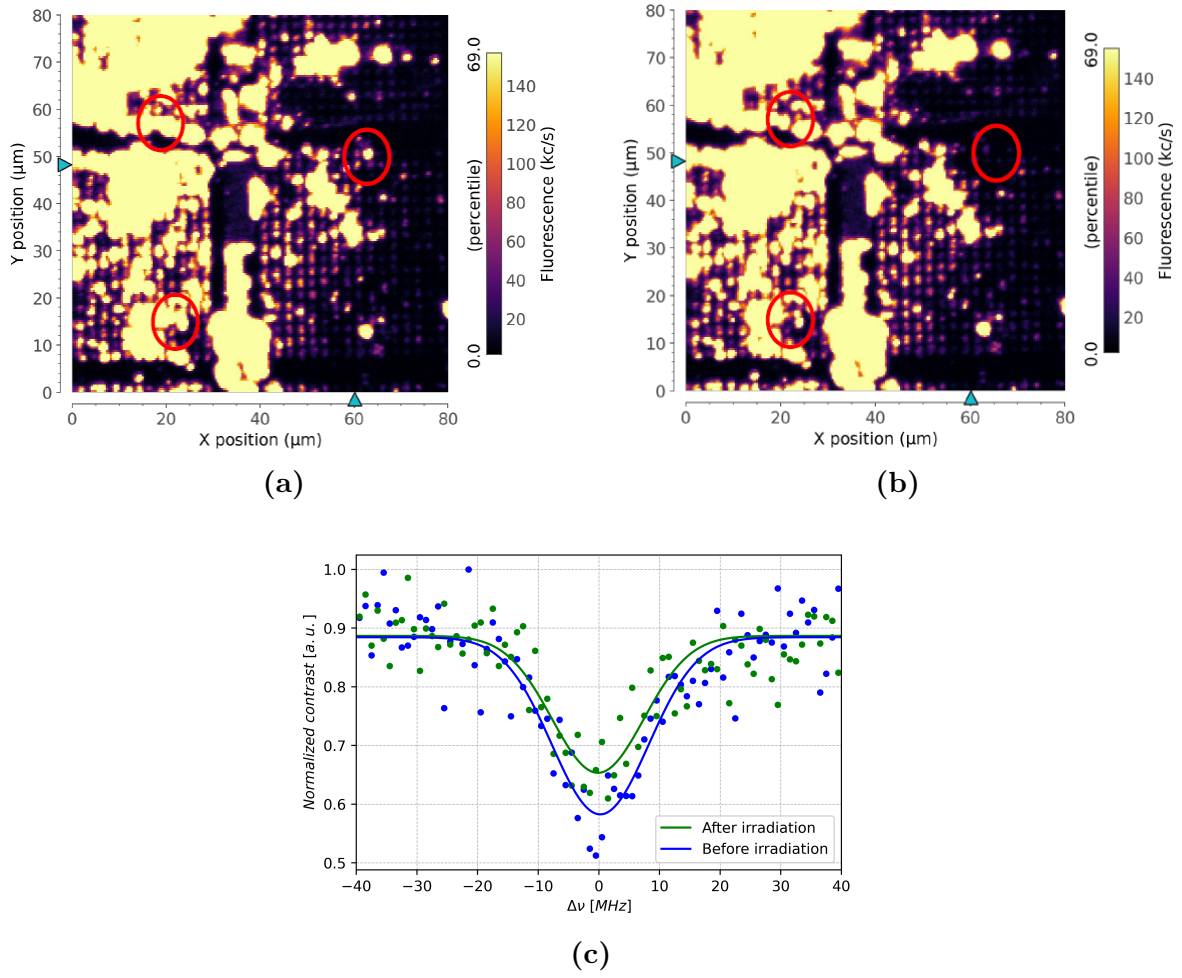

Figure 3.6: The effect of irradiation. **(a)** The diamond confocal image obtained before prolonged irradiation. One can observe the fluorescence material (bright clusters) originated from the drop-casting of the spin label OXYL-1-NHS in DMSO. **(b)** The confocal image obtained after prolonged irradiation at several spots (indicated with red circles) where one can observe the "disappearance" of the material (known as photo-bleaching), which causes the spot to become darker. **(c)** NV-based DEER signal obtained before (in blue) and after (in green) irradiating an NV center with a 520 nm laser diode. A decrease of 30% in the peak depth is observed. The spot was irradiated for 2 hours with a laser power of ≈1 mW. The detuning is from a resonance frequency of 1.5073 GHz, and 1.4935 GHz for the blue and the green fits respectively.

In Fig. 3.6c, one can observe the change in the signal intensity (≈ 30%) after prolonged laser

irradiation (≈1 mW for 2 hr). The intensity of the green curve (after prolonged irradiation) is lower than the intensity of the blue curve (before prolonged irradiation), probably due to the irradiation process. This effect was also observed while performing Raman spectroscopy measurements, and after examining the microscopic images of the samples (see Appendix, Sec. 5.1).

The spin labels are basically stable before being exposed to laser irradiation, as was investigated by X-band EPR measurement at RT. A possible explanation for the process is the photobleaching process which is induced by the 520 nm laser. This phenomenon was already observed in fluorescence microscopy [74] and here we have tried to quantify its influence.

4 Summary and Discussion

In this thesis, NV-based EPR spectroscopy of spin labels was performed. It involved using a homemade RT setup with which we have managed to obtain a DEER signal from nearby spin labels.

Firstly, we have successfully labeled poly-L-lysine with the nitroxide spin label OXYL-1-NHS. This was confirmed from CW EPR measurements where a difference in the height of the hyperfine peaks of the free label and the labeled peptide could be observed (see Fig. 3.1b). Secondly, we have managed to apply a tiny drop of the obtained labeled PLL solution accurately, with a spatial resolution of $\approx$ 100 µm. This resolution is important because it enables us to detect the material with our setup after performing the drop-casting process, and the evaporation of the drop is achieved. However, because it was difficult to detect the labeled peptides magnetically, probably because of the small concentration of covalently attached spin labels (only $\sim$15% of the lysines are to be labeled, as described in Sec. 3.1.1). Therefore, we decided to examine the spin label solution ($\sim$0.5 mg/ml), where we have a higher concentration of spins, and eventually managed to obtain DEER signals successfully (For achieving higher concentration of spin labels at the surface of diamond we also tried to perform covalent binding of spin labels to it, as described in Appendix, Sec. 5.2, where the preliminary results are shown). Then, we examined the influence of laser irradiation on the DEER signal and managed to observe a 30% decrease in the signal intensity (as shown in Fig. 3.6c). Moreover, the confocal scans before and after prolonged laser irradiation corroborate this result as shown in Fig. 3.6a and Fig. 3.6b, respectively. This effect could also be observed when performing Raman microscopy for the samples and by observing microscopic images that were taken before and after irradiation with a green laser (as described in Appendix, Sec. 5.1).

The discussed irradiation effect should be investigated more thoroughly in order to get more quantitative results that might help in realizing the scope of the effect, enable to characterize it, and achieve optimal measurement conditions. Moreover, DEER signals from spin-labeled peptides should be examined and analyzed in light of the discussed effect. Furthermore, another proposed technique to overcome the effect is the use of metallic layers, which are very reflective, that should be efficient for protecting the sample from exposure to laser irradiation during NV-based EPR measurements.

5 Appendix

5.1 Raman spectroscopy measurements

In order to investigate the effect of laser irradiation, we also used Raman spectroscopy which utilizes a confocal microscope (LabRAM HR, HORIBA) that enables diffraction-limited spatial resolution. We prepared a sample of the nitroxide radical 3-carboxy-PROXYL in methanol (5 mM) and drop cast it on a glass slide. After irradiating the sample with a 532 nm laser (0.864 mW) for 1 hour, a change in the appearance of the material could be observed. This is depicted in Fig. 5.1, when comparing micrographs 5.1a and 5.1b. We can see that, at the spot that was irradiated, a hole was created, probably due to a photobleaching process.

We also investigated the Raman spectra before (in red) and after (in green) the laser irradiation as depicted in sub-fig. 5.1c. Interestingly, as can be seen, several peaks have disappeared while other peaks have emerged. This effect is probably due to different phonon modes resulting from chemical changes occurring during the irradiation process.

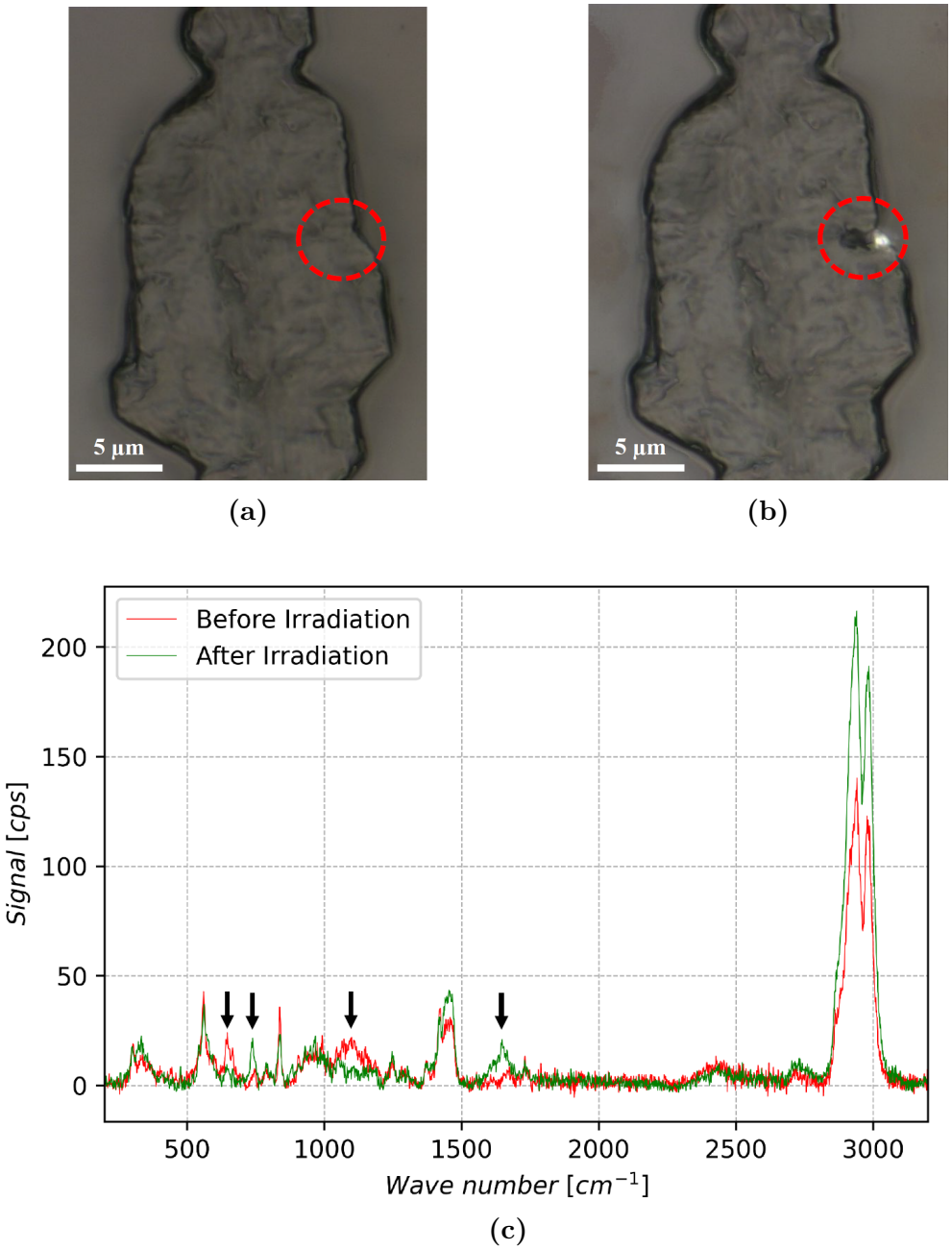

Figure 5.1: Raman measurement. **(a)** Micrograph of 3-carboxy-PROXYL cluster prior to laser irradiation. **(b)** Micrograph of the same 3-carboxy-PROXYL cluster after irradiation with 532 nm laser (0.864 mW) for 1hr. One can observe the damage to the cluster and the hole created at the spot where the laser beam was focused. **(c)** Raman spectra taken before (in red) and after (in green) the irradiation. One can observe the disappearance and emergence of several peaks (indicated by the black arrows), which apparently derive from different phonon-modes created due to chemical changes as a result of the irradiation process.

5.2 X-ray photoelectron spectroscopy (XPS) measurements

In order to enable better detection of spin labels, we tried to perform covalent binding of them to the diamond surface. Theoretically, this process can be performed by linking a spin label through the carboxylic group existing at the surface of an acid-treated diamond [75–77]. This can enable a better linkage than that we would get by using the drop-casting method where the interaction is based on van der Waals forces. Moreover, in the covalent binding method, we can achieve better proximity between an NV and the spin labels because of a shorter bond length, and because we can get rid of solvents more easily (in the drop-casting method, the solvent molecules might distance the spin labels from the surface, making them further from the NVs).

In order to perform the covalent binding of spin labels, we utilized two methods. In the first method, we tried to link a molecular linker to the diamond surface, and link the spin label molecule to the linker itself. The linker, in this case, is cystamine, and the spin label is MTSL. The reaction was performed under inert conditions (nitrogen gas) due to the susceptibility of cystamine to ambient conditions. 100 mg of cystamine were added to a flask containing 10 ml of triple distilled water (TDW) and the diamond sample. Later on, 50 mg of EDC (a carboxyl activating agent for the coupling of amines to yield amide bonds) were added in five iterations (10 mg each time) every one hour. The pH during the reaction was maintained at 4-6 to enable efficient conditions for the reaction. Afterward, the diamond was washed with TDW, dried, and kept under nitrogen gas. The second part of the reaction (liking MTSL to the linker) was not performed yet because we had to verify first that the first stage was successful. In the second method, we tried to bind the spin label molecule 4-amino-TEMPO directly to the surface of the diamond through the amine group of the 4-amino-TEMPO and the carboxylic group of the diamond. This reaction was performed the same way as the previous reaction except that cystamine was replaced with 4-amino-TEMPO and the fact that the reaction was performed at ambient conditions.

The obtained samples from the two experiments were examined with XPS. Moreover, a reference sample (clean diamond) and a control sample that was cleaned after being in a solution of EDC were examined. Fig. 5.2e depicts the XPS results. We examined the signal achieved due to electrons from the 1s orbital of nitrogen (395-410 eV) and tried to deduce the species existing at the diamond surface. In sub-fig. 5.2a, one can observe the signal achieved from a reference diamond sample. A small peak can be observed due to a relatively small concentration of nitrogen (0.55% as shown in table 1). However, in the rest of the samples, the concentration of nitrogen was higher due to the performed treatments (see table 1). Although it could be a good indication for the existence of the desired material, these signals from nitrogen probably derived mainly from EDC, which gave a prominent signal (see sub-fig. 5.2e). In sub-fig. 5.2d, we can see a fit to the raw data (in red) comprised from the sum of three components of Gaussian-Lorentzian functions (70% Gaussian and

30% Lorentzian each). These three components probably stem from the 3 different nitrogen atoms of the EDC molecule, which have different oxidation states. However, their area ratio is not equal (i.e., 1:1:1), probably due to other nitrogen sources (from the diamond surface itself, for instance). These 3 components also gave a good fit to the rest of the graphs, as can be seen in sub-fig. 5.2b and sub-fig. 5.2c (Although the area ratios are a bit different in each of them).

In conclusion, from the XPS measurement, the binding of 4-amino-TEMPO or cystamine to the surface of diamond is nonconclusive. However, for some reason which is not yet clear, EDC seems to attach relatively well to the surface of the diamond.

Sample	Reference	4-Amino-TEMPO	Cystamine	EDC
Nitrogen atomic conc.(%)	0.55%	2.03%	1.57%	2.5%

Table 1: Nitrogen atomic concentration (%) in the different samples. These concentrations were calculated based on the normalized area of the nitrogen peak divided by its relative sensitivity factor (RSF).

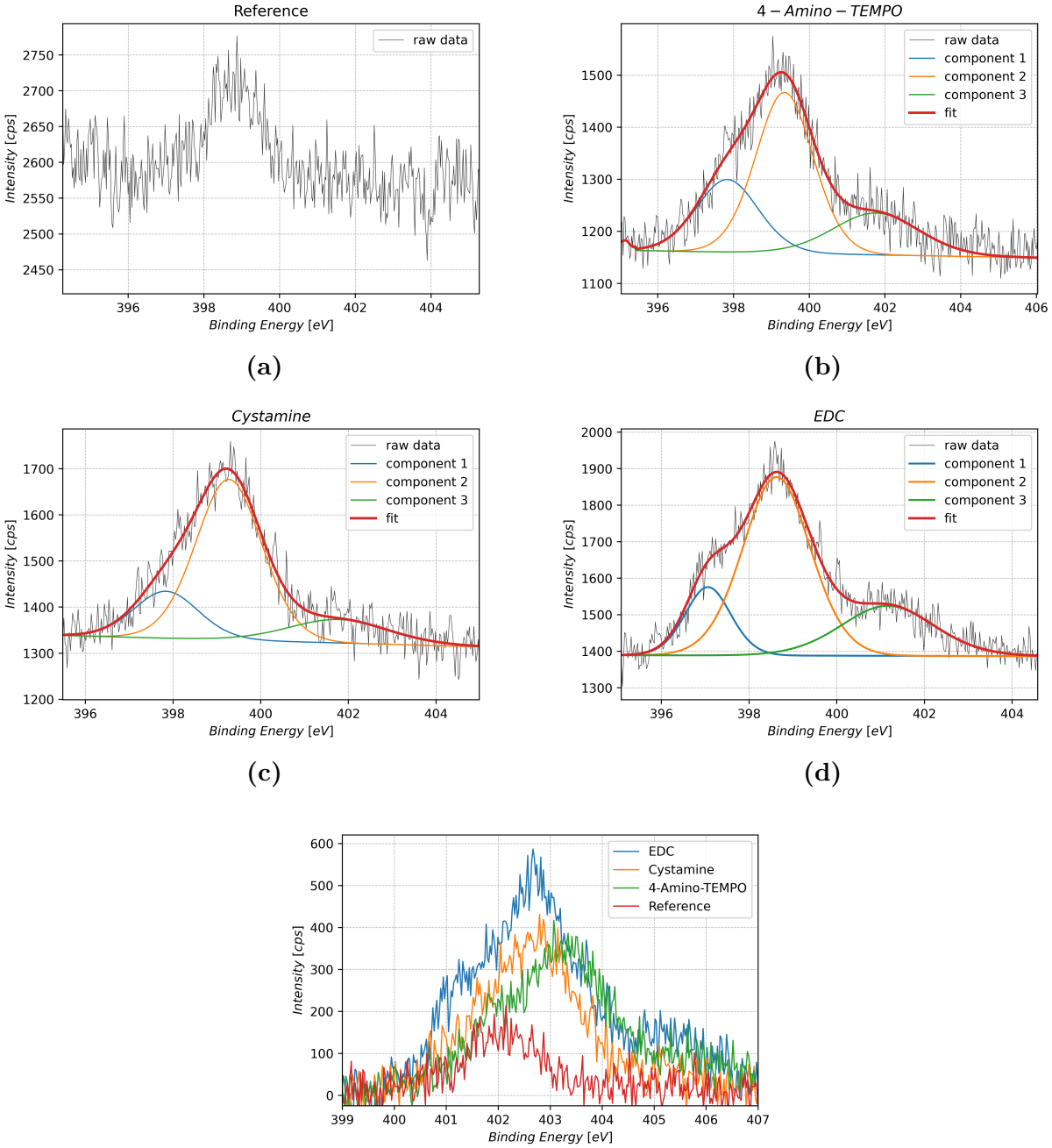

Figure 5.2: XPS measurements. Comparing the signals stemmed from nitrogen species (emission from 1s orbital, at 395-410 eV) located at the surface of treated and untreated diamonds (5mm x 5mm x 0.3 mm). **(a)** The XPS signal obtained from the reference sample (acid cleaned diamond). One can observe a relatively small peak. **(b)** XPS signal of 4-Amino-TEMPO treated sample. One can observe the three components used to fit the data (70% Gaussian and 30% Lorentzian) based on the different nitrogen species (different oxidation states). The total fit (in red) is the sum of all the components. **(c)** XPS signal of cystamine treated sample. One can observe the three components used to fit the data based on the different nitrogen species. The total fit (in red) is the sum of all the components. **(d)** XPS signal of EDC treated sample. One can observe the three components used to fit the data based on the different nitrogen species. The total fit (in red) is the sum of all the components. **(e)** Raw data of the different samples. One can observe that the signal obtained from the reference sample is weak while the signal of the EDC is prominent and might be the source for the signal in all other samples where this material was used as an activator for the covalent bonding reaction to carboxylic groups at the diamond surface.

References

[1] John C Kendrew, G Bodo, Howard M Dintzis, RG Parrish, Harold Wyckoff, and David C Phillips. A three-dimensional model of the myoglobin molecule obtained by x-ray analysis. *Nature*, 181(4610):662–666, 1958.

[2] Andrea Ilari and Carmelinda Savino. Protein structure determination by x-ray crystallography. *Bioinformatics*, pages 63–87, 2008.

[3] T. A. Cross and S. J. Opella. Protein structure by solid-state NMR. *Journal of the American Chemical Society*, 105(2):306–308, 1983.

[4] Christiane R Timmel and Jeffrey R Harmer. *Structural Information from Spin-Labels and Intrinsic Paramagnetic Centres in the Biosciences*, volume 152. Springer, 2014.

[5] A. Lozovoi, D. Daw, H. Jayakumar, and C. A. Meriles. Dark defect charge dynamics in bulk chemical-vapor-deposition-grown diamonds probed via nitrogen vacancy centers. *Phys. Rev. Materials*, 4:053602, May 2020.

[6] Shang Li, Huijie Zheng, Zaili Peng, Mizuki Kamiya, Tomoyuki Niki, Viktor Stepanov, Andrey Jarmola, Yasuhiro Shimizu, Susumu Takahashi, Arne Wickenbrock, and Dmitry Budker. Determination of local defect density in diamond by double electron-electron resonance, 2021.

[7] Bernhard Grotz, Johannes Beck, Philipp Neumann, Boris Naydenov, Rolf Reuter, Friedemann Reinhard, Fedor Jelezko, Jörg Wrachtrup, David Schweinfurth, Biprajit Sarkar, and Philip Hemmer. Sensing external spins with nitrogen-vacancy diamond. *New J. Phys.*, 13:055004, 2011.

[8] H. J. Mamin, M. H. Sherwood, and D. Rugar. Detecting external electron spins using nitrogen-vacancy centers. *Phys. Rev. B*, 86:195422, 2012.

[9] Fazhan Shi, Qi Zhang, Pengfei Wang, Hongbin Sun, Jiarong Wang, Xing Rong, Ming Chen, Chenyong Ju, Friedemann Reinhard, Hongwei Chen, Jörg Wrachtrup, Junfeng Wang, and Jiangfeng Du. Single-protein spin resonance spectroscopy under ambient conditions. *Science*, 347:1135–1138, 2015.

[10] Lukas Schlipf, Thomas Oeckinghaus, Kebiao Xu, Durga Bhaktavatsala Rao Dasari, Andrea Zappe, Felipe Fávaro de Oliveira, Bastian Kern, Mykhailo Azarkh, Malte Drescher, Markus Ternes, Klaus Kern, Jörg Wrachtup, and Amit Finkler. Molecular quantum spin network controlled by a single qubit. *Sci. Adv.*, 3:e1701116, 2017.

[11] Chris J.H. Wort and Richard S. Balmer. Diamond as an electronic material. *Materials Today*, 11(1):22–28, 2008.

[12] FP Bundy, H Tracy Hall, HM Strong, and RH Wentorfjun. Man-made diamonds. *nature*, 176(4471):51–55, 1955.

[13] M Werner and R Locher. Growth and application of undoped and doped diamond films. *Reports on Progress in Physics*, 61(12):1665–1710, dec 1998.

[14] Yang Zhang, Zhonghao Li, Yuanyao Feng, Hao Guo, Huanfei Wen, Jun Tang, and Jun Liu. High-sensitivity dc magnetic field detection with ensemble nv centers by pulsed quantum filtering technology. *Opt. Express*, 28(11):16191–16201, May 2020.

[15] Gopalakrishnan Balasubramanian, Philipp Neumann, Daniel Twitchen, Matthew Markham, Roman Kolesov, Norikazu Mizuochi, Junichi Isoya, Jocelyn Achard, Johannes Beck, Julia Tisler, Vincent Jacques, Philip R. Hemmer, Fedor Jelezko, and Jörg Wrachtrup. Ultralong spin coherence time in isotopically engineered diamond. *Nat. Mater.*, 8:383–387, 2009.

[16] Marcus W. Doherty, Neil B. Manson, Paul Delaney, Fedor Jelezko, Jörg Wrachtrup, and Lloyd C.L. Hollenberg. The nitrogen-vacancy colour centre in diamond. *Phys. Rep.*, 528(1):1–45, 2013. The nitrogen-vacancy colour centre in diamond.

[17] Mark Fox. Optical properties of solids, 2002.

[18] T. Rosskopf, A. Dussaux, K. Ohashi, M. Loretz, R. Schirhagl, H. Watanabe, S. Shikata, M. Itoh, K. and L. Degen, C.˙ Investigation of surface magnetic noise by shallow spins in diamond. *Phys. Rev. Lett.*, 112:147602, 2014.

[19] A. Jarmola, V. M. Acosta, K. Jensen, S. Chemerisov, and D. Budker. Temperature- and magnetic-field-dependent longitudinal spin relaxation in nitrogen-vacancy ensembles in diamond. *Phys. Rev. Lett.*, 108:197601, 2012.

[20] D. A. Redman, S. Brown, R. H. Sands, and S. C. Rand. Spin dynamics and electronic states of N-V centers in diamond by EPR and four-wave-mixing spectroscopy. *Phys. Rev. Lett.*, 67:3420–3423, Dec 1991.

[21] A. Lenef and S. C. Rand. Electronic structure of the N-V center in diamond: Theory. *Phys. Rev. B*, 53:13441–13455, May 1996.

[22] N. B. Manson, J. P. Harrison, and M. J. Sellars. Nitrogen-vacancy center in diamond: Model of the electronic structure and associated dynamics. *Phys. Rev. B*, 74:104303, 2006.

[23] P. Kehayias, M. W. Doherty, D. English, R. Fischer, A. Jarmola, K. Jensen, N. Leefer, P. Hemmer, N. B. Manson, and D. Budker. Infrared absorption band and vibronic

structure of the nitrogen-vacancy center in diamond. *Phys. Rev. B*, 88:165202, Oct 2013.

[24] Churna Bhandari, Aleksander L. Wysocki, Sophia E. Economou, Pratibha Dev, and Kyungwha Park. Multiconfigurational study of the negatively charged nitrogen-vacancy center in diamond. *Phys. Rev. B*, 103:014115, Jan 2021.

[25] Gordon Davies and MF Hamer. Optical studies of the 1.945 eV vibronic band in diamond. *Proceedings of the Royal Society of London. A. Mathematical and Physical Sciences*, 348(1653):285–298, 1976.

[26] M. L. Goldman, M. W. Doherty, A. Sipahigil, N. Y. Yao, S. D. Bennett, N. B. Manson, A. Kubanek, and M. D. Lukin. State-selective intersystem crossing in nitrogen-vacancy centers. *Phys. Rev. B*, 91:165201, 2015.

[27] M. L. Goldman, A. Sipahigil, M. W. Doherty, N. Y. Yao, S. D. Bennett, M. Markham, D. J. Twitchen, N. B. Manson, A. Kubanek, and M. D. Lukin. Phonon-induced population dynamics and intersystem crossing in nitrogen-vacancy centers. *Phys. Rev. Lett.*, 114(14), April 2015.

[28] L Rondin, J-P Tetienne, T Hingant, J-F Roch, P Maletinsky, and V Jacques. Magnetometry with nitrogen-vacancy defects in diamond. *Rep. Prog. Phys.*, 77(5):056503, 2014.

[29] Romana Schirhagl, Kevin Chang, Michael Loretz, and Christian L. Degen. Nitrogen-vacancy centers in diamond: Nanoscale sensors for physics and biology. *Annu. Rev. Phys. Chem.*, 65(1):83, 2014. PMID: 24274702.

[30] Vincent Jacques, JD Murray, François Marquier, Dominique Chauvat, Frédéric Grosshans, François Treussart, and J-F Roch. Enhancing single-molecule photostability by optical feedback from quantum jump detection. *Applied Physics Letters*, 93(20):422, 2008.

[31] Benoit Mahler, Piernicola Spinicelli, Stephanie Buil, Xavier Quelin, Jean-Pierre Hermier, and Benoit Dubertret. Towards non-blinking colloidal quantum dots. *Nature materials*, 7(8):659–664, 2008.

[32] Pengfei Wang, Sanyou Chen, Maosen Guo, Shijie Peng, Mengqi Wang, Ming Chen, Wenchao Ma, Rui Zhang, Jihu Su, Xing Rong, Fazhan Shi, Tao Xu, and Jiangfeng Du. Nanoscale magnetic imaging of ferritins in a single cell. *Sci. Adv.*, 5(4):eaau8038, April 2019.

[33] Yuzhou Wu, Fedor Jelezko, Martin B Plenio, and Tanja Weil. Diamond quantum devices in biology. *Angew. Chem. Int. Ed.*, 55(23):6586–6598, 2016.

[34] David A Simpson, Emma Morrisroe, Julia M McCoey, Alain H Lombard, Dulini C Mendis, Francois Treussart, Liam T Hall, Steven Petrou, and Lloyd CL Hollenberg. Non-neurotoxic nanodiamond probes for intraneuronal temperature mapping. *ACS nano*, 11(12):12077–12086, 2017.

[35] Akihiro Kuwahata, Takahiro Kitaizumi, Kota Saichi, Takumi Sato, Ryuji Igarashi, Takeshi Ohshima, Yuta Masuyama, Takayuki Iwasaki, Mutsuko Hatano, Fedor Jelezko, et al. Magnetometer with nitrogen-vacancy center in a bulk diamond for detecting magnetic nanoparticles in biomedical applications. *Scientific reports*, 10(1):1–9, 2020.

[36] James L Webb, Luca Troise, Nikolaj W Hansen, Jocelyn Achard, Ovidiu Brinza, Robert Staacke, Michael Kieschnick, Jan Meijer, Jean-François Perrier, Kirstine Berg-Sørensen, et al. Optimization of a diamond nitrogen vacancy centre magnetometer for sensing of biological signals. *Frontiers in Physics*, 8:430, 2020.

[37] Jan Barton, Michal Gulka, Jan Tarabek, Yuliya Mindarava, Zhenyu Wang, Jiri Schimer, Helena Raabova, Jan Bednar, Martin B Plenio, Fedor Jelezko, et al. Nanoscale dynamic readout of a chemical redox process using radicals coupled with nitrogen-vacancy centers in nanodiamonds. *ACS nano*, 14(10):12938–12950, 2020.

[38] Gopalakrishnan Balasubramanian, I. Y. Chan, Roman Kolesov, Mohannad Al-Hmoud, Julia Tisler, Chang Shin, Changdong Kim, Aleksander Wojcik, Philip R. Hemmer, Anke Krueger, Tobias Hanke, Alfred Leitenstorfer, Rudolf Bratschitsch, Fedor Jelezko, and Jörg Wrachtrup. Nanoscale imaging magnetometry with diamond spins under ambient conditions. *Nature*, 455:648–651, 2008.

[39] Francesco Casola, Toeno van der Sar, and Amir Yacoby. Probing condensed matter physics with magnetometry based on nitrogen-vacancy centres in diamond. *Nature Reviews Materials*, 3:17088, 2018.

[40] J-P Tetienne, L Rondin, P Spinicelli, M Chipaux, T Debuisschert, J-F Roch, and V Jacques. Magnetic-field-dependent photodynamics of single NV defects in diamond: an application to qualitative all-optical magnetic imaging. *New J. Phys.*, 14:103033, 2012.

[41] Jörg Wrachtrup and Amit Finkler. Single spin magnetic resonance. *J. Magn. Reson.*, 269:225–236, 2016.

[42] Fazhan Shi, Fei Kong, Pengju Zhao, Xiaojun Zhang, Ming Chen, Sanyou Chen, Qi Zhang, Mengqi Wang, Xiangyu Ye, Zhecheng Wang, Zhuoyang Qin, Xing Rong,

Jihu Su, Pengfei Wang, Peter Z. Qin, and Jiangfeng Du. Single-DNA electron spin resonance spectroscopy in aqueous solutions. *Nat. Methods*, 2018.

[43] Philip Hemmer and Carmen Gomes. Single proteins under a diamond spotlight. *Science*, 347(6226):1072–1073, 2015.

[44] S. Felton, A. M. Edmonds, M. E. Newton, P. M. Martineau, D. Fisher, D. J. Twitchen, and J. M. Baker. Hyperfine interaction in the ground state of the negatively charged nitrogen vacancy center in diamond. *Phys. Rev. B*, 79(7), 2009.

[45] Benjamin Smeltzer, Jean McIntyre, and Lilian Childress. Robust control of individual nuclear spins in diamond. *Phys. Rev. A*, 80:050302, Nov 2009.

[46] S. Bandyopadhyay and M. Cahay. *Introduction to Spintronics, Second Edition*. Taylor & Francis, 2015.

[47] J Robert Johansson, Paul D Nation, and Franco Nori. Qutip: An open-source python framework for the dynamics of open quantum systems. *Computer Physics Communications*, 183(8):1760–1772, 2012.

[48] I. I. Rabi, N. F. Ramsey, and J. Schwinger. Use of rotating coordinates in magnetic resonance problems. *Rev. Mod. Phys.*, 26:167–171, Apr 1954.

[49] E Van Oort, NB Manson, and M Glasbeek. Optically detected spin coherence of the diamond NV centre in its triplet ground state. *Journal of Physics C: Solid State Physics*, 21(23):4385, 1988.

[50] A. Dréau, M. Lesik, L. Rondin, P. Spinicelli, O. Arcizet, J.-F. Roch, and V. Jacques. Avoiding power broadening in optically detected magnetic resonance of single NV defects for enhanced dc magnetic field sensitivity. *Phys. Rev. B*, 84:195204, November 2011.

[51] Marina Brustolon and Elio Giamello. *Electron Paramagnetic Resonance: A Practitioners Toolkit*. John Wiley & Sons, 2009.

[52] John F. Barry, Jennifer M. Schloss, Erik Bauch, Matthew J. Turner, Connor A. Hart, Linh M. Pham, and Ronald L. Walsworth. Sensitivity optimization for NV-diamond magnetometry. *Rev. Mod. Phys.*, 92:015004, Mar 2020.

[53] Benjamin Smeltzer, Lilian Childress, and Adam Gali. ^{13}C hyperfine interactions in the nitrogen-vacancy centre in diamond. *New J. Phys.*, 13(2):025021, 2011.

[54] J. M. Taylor, P. Cappellaro, L. Childress, L. Jiang, D. Budker, P. R. Hemmer, A. Yacoby, R. Walsworth, and M. D. Lukin. High-sensitivity diamond magnetometer with nanoscale resolution. *Nat. Phys.*, 4:810–816, 2008.

[55] E. L. Hahn. Spin echoes. *Phys. Rev.*, 80:580–594, 1950.

[56] C.P. Slichter. *Principles of Magnetic Resonance*. Springer Series in Solid-State Sciences. Springer Berlin Heidelberg, 1996.

[57] Lan Luan, Michael S. Grinolds, Sungkun Hong, Patrick Maletinsky, Ronald L. Walsworth, and Amir Yacoby. Decoherence imaging of spin ensembles using a scanning single-electron spin in diamond. *Sci. Rep.*, 5:8119, 2015.

[58] H. J. Mamin, M. Kim, M. H. Sherwood, C. T. Rettner, K. Ohno, D. D. Awschalom, and D. Rugar. Nanoscale nuclear magnetic resonance with a nitrogen-vacancy spin sensor. *Science*, 339:557–560, 2013.

[59] L. Childress, M. V. Gurudev Dutt, J. M. Taylor, A. S. Zibrov, F. Jelezko, J. Wrachtrup, P. R. Hemmer, and M. D. Lukin. Coherent dynamics of coupled electron and nuclear spin qubits in diamond. *Science*, 314(5797):281–285, 2006.

[60] Jonas Meinel, Vadim Vorobyov, Boris Yavkin, Durga Dasari, Hitoshi Sumiya, Shinobu Onoda, Junichi Isoya, and Jörg Wrachtrup. Heterodyne sensing of microwaves with a quantum sensor. *Nature communications*, 12(1):1–8, 2021.

[61] Andrew Horsley, Patrick Appel, Janik Wolters, Jocelyn Achard, Alexandre Tallaire, Patrick Maletinsky, and Philipp Treutlein. Microwave device characterization using a widefield diamond microscope. *Phys. Rev. Applied*, 10:044039, Oct 2018.

[62] R. Hanbury Brown and R. Q. Twiss. Correlation between photons in two coherent beams of light. *Nature*, 177(4497):27–29, January 1956.

[63] Raanan Carmieli, Niv Papo, Herbert Zimmermann, Alexey Potapov, Yechiel Shai, and Daniella Goldfarb. Utilizing ESEEM spectroscopy to locate the position of specific regions of membrane-active peptides within model membranes. *Biophysical Journal*, 90(2):492–505, 2006.

[64] Sriram Mahesh, Kuei-Chien Tang, and Monika Raj. Amide bond activation of biological molecules. *Molecules*, 23(10):2615, 2018.

[65] S. Ali Momenzadeh, Rainer J. Stöhr, Felipe Fávaro de Oliveira, Andreas Brunner, Andrej Denisenko, Sen Yang, Friedemann Reinhard, and Jörg Wrachtrup. Nanoengineered diamond waveguide as a robust bright platform for nanomagnetometry using shallow nitrogen vacancy centers. *Nano Lett.*, 15:165–169, 2014.

[66] S. Meiboom and D. Gill. Modified spin-echo method for measuring nuclear relaxation times. *Rev. Sci. Instrum.*, 29:688, 1958.

[67] A.A Maudsley. Modified Carr-Purcell-Meiboom-Gill sequence for NMR fourier imaging applications. *Journal of Magnetic Resonance (1969)*, 69(3):488–491, 1986.

[68] Terry Gullion and Jacob Schaefer. Elimination of resonance offset effects in rotational-echo, double-resonance NMR. *Journal of Magnetic Resonance (1969)*, 92(2):439–442, 1991.

[69] P. Neumann, N. Mizuochi, F. Rempp, P. Hemmer, H. Watanabe, S. Yamasaki, V. Jacques, T. Gaebel, F. Jelezko, and J. Wrachtrup. Multipartite entanglement among single spins in diamond. *Science*, 320:1326, 2008.

[70] M. Steiner, P. Neumann, J. Beck, F. Jelezko, and J. Wrachtrup. Universal enhancement of the optical readout fidelity of single electron spins at nitrogen-vacancy centers in diamond. *Phys. Rev. B*, 81:035205, January 2010.

[71] Magdalena Solà-Garcia, Sophie Meuret, Toon Coenen, and Albert Polman. Electron-induced state conversion in diamond NV centers measured with pump–probe cathodoluminescence spectroscopy. *ACS photonics*, 7(1):232–240, 2019.

[72] L. Rondin, G. Dantelle, A. Slablab, F. Grosshans, F. Treussart, P. Bergonzo, S. Perruchas, T. Gacoin, M. Chaigneau, H.-C. Chang, V. Jacques, and J.-F. Roch. Surface-induced charge state conversion of nitrogen-vacancy defects in nanodiamonds. *Phys. Rev. B*, 82(11), September 2010.

[73] M. V. Hauf, B. Grotz, B. Naydenov, M. Dankerl, S. Pezzagna, J. Meijer, F. Jelezko, J. Wrachtrup, M. Stutzmann, F. Reinhard, and J. A. Garrido. Chemical control of the charge state of nitrogen-vacancy centers in diamond. *Phys. Rev. B*, 83:081304, Feb 2011.

[74] Alberto Diaspro, Giuseppe Chirico, Cesare Usai, Paola Ramoino, and Jurek Dobrucki. Photobleaching. In *Handbook of biological confocal microscopy*, pages 690–702. Springer, 2006.

[75] Sorawis Sangtawesin, Bo L. Dwyer, Srikanth Srinivasan, James J. Allred, Lila V. H. Rodgers, Kristiaan De Greve, Alastair Stacey, Nikolai Dontschuk, Kane M. O'Donnell, Di Hu, D. Andrew Evans, Cherno Jaye, Daniel A. Fischer, Matthew L. Markham, Daniel J. Twitchen, Hongkun Park, Mikhail D. Lukin, and Nathalie P. de Leon. Origins of diamond surface noise probed by correlating single-spin measurements with surface spectroscopy. *Phys. Rev. X*, 9:031052, 2019.

[76] Robert G Ryan, Alastair Stacey, Kane M O'Donnell, Takeshi Ohshima, Brett C Johnson, Lloyd CL Hollenberg, Paul Mulvaney, and David A Simpson. Impact of surface

functionalization on the quantum coherence of nitrogen-vacancy centers in nanodiamonds. *ACS applied materials and interfaces*, 10(15):13143–13149, 2018.

[77] Benjamin F Bachman, Zachary R Jones, Gabriel R Jaffe, Jad Salman, Raymond Wambold, Zhaoning Yu, Jennifer T Choy, Shimon J Kolkowitz, Mark A Eriksson, Mikhail A Kats, et al. High-density covalent grafting of spin-active molecular moieties to diamond surfaces. *Langmuir*, 37(30):9222–9231, 2021.

Acknowledgements

Working on this thesis was very exciting and great, although the many challenges that arose during it. In the beginning, it seemed almost impossible to perform this work and become familiarized with the scientific field and the innovative homemade instrumentations. However, with a lot of effort and persistence and help and support from others, it became feasible.

First, I would like to thank Dr. Amit Finkler for giving me the opportunity to work on this interesting project and his obliging support throughout my thesis, which improved me a lot. Second, I would like to thank Inbar Zohar for guiding me in my work on the setup she built, explaining every detail, and helping with everything that was needed. I would also like to thank Dr. Jitender Kumar, Dan Yudilevich, and Leora Schein-Lubomirsky for the thoughtful discussions and the support and help in every issue. Moreover, I would like to thank Dr. Raanan Carmieli for helping me with the EPR measurements, the great consulting, and the interesting discussions. I would also like to thank Dr. Iddo Pinkas for the generous help with the Raman measurements and laser-related subjects. Furthermore, I would like to thank Dr. Andrea Zappe for technical support with the spin labeling process and Dr. Hagai Cohen for helping with surface chemistry subjects and with the XPS measurements.